Ph. D. Dissertion

Development of Microfluidic Platform with Through-polydimethylsiloxane Microtip Electrode Array for Photosynthetic Microbial Fuel Cell

광합성 미생물 연료 전지 구현을 위한 폴리디메틸실록세인 관통 미세 탐침 전극 어레이의 개발

2017 년 8 월

서울대학교 대학원

전기 컴퓨터 공학부

하 준 근

Development of Microfluidic Platform with Through-polydimethylsiloxane Microtip Electrode Array for Photosynthetic Microbial Fuel Cell

지도 교수 김 용 권

이 논문을 공학박사 학위논문으로 제출함

2017 년 8 월

서울대학교 대학원

전기 컴퓨터 공학부

하 준 근

하준근의 공학박사 학위논문을 인준함

2017 년 8 월

위 원 장 _____ (인)

부위원장 _____ (인)

위 원 _____ (인)

위 원 _____ (인)

위 원 _____ (인)

Abstract

This dissertation proposes and realizes microfluidic platform with through-polydimethylsiloxane microtip electrode array applicable to array level microbial fuel cell. Conventional single cell based insertion methods have drawbacks of low efficiency power extraction. In order to overcome this disadvantage, we aimed to extract power from a stacked cell array using microtip electrode insertion method and microfluidic device fabrication technology. The ultramicroelectrode (UME) on the microtips and an electrode inside the microfluidic chamber were used as an anode and a cathode for the microbial fuel cell, respectively. After the UME was inserted into an array of photosynthetic cells immobilized in the microfluidic chamber, electrons generated during photosynthesis were extracted via the UMEs on the invasive microtips, and were reduced on the cathode in the microfluidic chamber.

Integration of UMEs on silicon microtip is proposed with the detailed analysis and verified with the fabrication results of a conductive microtip array having localized UMEs at the tip end. In order to use a microtip electrode in penetrating applications, a study on the variation of electrode design is necessary. A silicon microtip is fabricated using a combination of DRIE and sulfur hexafluoride (SF_6) RIE steps. The shape of the microtip is transformed from pillar type to tip type by the variation of the sidewall etching rate of the pillar in the SF_6 RIE step. The aspect ratio and the apex radius of the silicon microtip are controlled by mask design with varying diameter and gap of etching mask patterns. A localized UME is formed at the end of the microtip by depositing and patterning the insulating layer without an additional photolithography step. After the fabrication, electrochemical

characterization of the UME was performed using cyclic voltammetry (CV), and compared with an estimation based on conical UME theory.

The photosynthetic algae cells are immobilized in microfluidic device by inserting the silicon-based electrode into the PDMS fluidic channel. This method is realized by penetrating the bottom thin film of the PDMS fluidic channel with sharp end of the electrode. For easy penetration, the electrode was fabricated in the form of sharp microtip and designed to be positioned in the channel by fabricating arrangement layer around the microtip electrode.

Short circuit current and open circuit voltage of the inserted electrode array were measured at 207 pA and 26 mV. Loss analysis of measured current values was done in two ways. First, the decrease of the measured current due to the distance between the working electrode and the counter electrode was verified by electrochemical simulation. As the distance between the working electrode and the counter electrode increases, the magnitude of the current due to the resistance of the electrolyte decreases. Second, it is the deformation of the PDMS thin film by the micro probe electrode moving in the vertical direction during the inserting process. In order to analyze the effect of deformation on the magnitude of the measurement current, the deformation due to the low strength of the thin PDMS thin film was measured and the effective width in the insertion process was calculated by deformation.

Simulation results show that the current value is about 53% of the measured value when the distance between electrodes is 5 μm (ideal value). As a result of the effective area calculation, the number of effective electrodes among the total number of 17689 electrodes is 946, and the measured current per electrode is 0.22 pA. If the effective electrode is assumed to have no current loss due to the distance

between the electrodes, the current value per electrode is calculated to be 0.40 pA.

In conclusion, this dissertation demonstrated the possibility of intracellular insertion of the electrode using the developed microtip electrode and the proposed through-polydimethylsiloxane assembly method. In addition, a short circuit current and an open circuit voltage measurement showed the possibility of being used as a microbial fuel cell. Based on the analysis of the loss of the measured results, a method of reducing the current loss by improving the electrode arrangement and the microfluidic structure was suggested.

주요어 : Microbial fuel cell, Ultramicroelectrode, Microtip electrode, Through-PDMS insertion method.

학 번 : 2010-31002

Table of contents

List of tables

List of figures

Chapter 1. Introduction

1.1. Backgrounds

In recent years, as interest in environmental issues increases significantly, the industrial world faced with necessity of conversion and reconstruction to environment-friendly structure because environmental regulations have tightened up. The technical innovations have progressed in variety fields related to environment such as environmental monitoring, diagnosis, analysis and control. In particular, development of clean energy that becomes the basis of all of the industry is essential for sustainable economic growth and international benefit. Direction of technological development of clean energy has focused on short-term approach such as energy saving and efficiency enhancement of existing energy industry.

1.1.1. Microbial fuel cell

Microbial fuel cells (MFCs) constitute an energy-harvesting system that uses the various metabolic processes of cells to convert chemical energy into electricity. Cells in the anodic chamber of the MFC generate electricity using catalytic reactions during the biodegradation of organic matter. Recently, MFC has been widely studied, since it is considered a cheap and environmentally friendly energy source [1, 2].

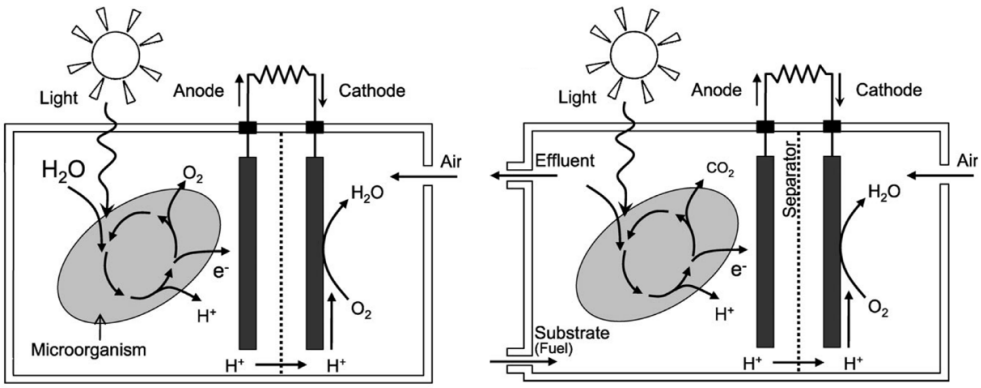

Figure 1-1. Setup of a (a) photosynthetic microbial fuel cell and a (b) microbial fuel cell [3].

The microbial fuel cell is composed of an oxidized electrode part and a reduced electrode part, and is separated by an ion exchange membrane. In the anaerobic oxidizing electrode part, microorganisms adhere to the surface of the electrode, and microorganisms in the wastewater injected from the outside are oxidized. Carbon dioxide, hydrogen ions and electrons are produced by the oxidation of microorganisms. The generated hydrogen ions move to the reduction electrode through the ion exchange membrane, and at the same time, electrons move from the oxidation electrode to the reduction electrode through the external circuit. This flow of electrons causes electric current to be generated. When the final electron acceptor present in the reducing electrode is oxygen, the transferred hydrogen ions and electrons combine to form water, and the reaction is terminated.

The substrates used in microbial fuel cells are mainly acetic acid, glucose, and propionic esters, which are the first electron donors in microbial fuel cells. A ferricyanide may be used as an electron acceptor to be injected into the reducing electrode portion existing in an aerobic state [4, 5]. The greatest advantage of ferricyanide is that they have low overpotentials [6]. However, ferricyanide is not

suitable for long-term operation because periodic insufficient reoxidation occurs and periodic replacement is necessary and the ferricyanide compound is diffused through the ion exchange membrane to negatively affect the oxidized electrode part. Recently, the use of oxygen as an electron acceptor has been increasing due to the researches on air cathode microbial fuel cells [7-11]. Oxygen is a highly efficient material that can compensate for the disadvantages of using ferricyanide compounds and has a high reducing electrode potential. Recently, research has been conducted on a bio-reducing electrode microbial fuel cell in which microbes are injected into an oxygen-free reducing electrode portion using nitrate as an electron accepting agent [12].

The ion exchange membrane used in the microbial fuel cell separates the two solutions in the oxidized electrode portion and the reduced electrode portion, and is called a separation membrane. It is known that the separation membrane moves the hydrogen ions produced by the oxidation reaction in the oxidation electrode portion to the reduction electrode portion [13]. However, when the microbial fuel cell is actually operated, the consumption rate of the hydrogen ion at the reducing electrode portion is higher than that of the hydrogen ion through the ion exchange membrane [14]. Also, in the case of a microbial fuel cell operating in an aqueous solution state, a large amount of positive ions existing in the catholyte liquid migrate to the reduction electrode portion through the ion exchange membrane, and the movement of hydrogen ions is disturbed [15]. To demonstrate this, Rozendal et al. analyzed the composition of the ion exchange membrane after operating a microbial fuel cell using an ion exchange membrane, Nafion 117 [15]. As a result, 74% of the sulfonic acid groups constituting the ion exchange membrane were bound to K and Na, respectively. The changes in the anions of the anolyte and the

catholyte were observed by Chae et. al. using a reactor in which the microorganisms were not propagated with 50 mM phosphate buffer [16]. As a result, it was confirmed that a large amount of cations such as K^+ and NH_4^+ migrated to the catholyte through the ion exchange membrane. This phenomenon is interpreted to be due to the fact that the concentration of the cation in the catholyte in the neutral state (pH 7) is higher than that of the hydrogen ion. Due to the difficulty of transferring such hydrogen ions through the ion exchange membrane, hydrogen ions are accumulated in the electrode portion. As a result, hydrogen ions are accumulated in the oxidized electrode portion, and the pH of the catholyte solution is decreased, which hinders the growth and activity of the microorganism. In addition, the hydrogen ions in the reducing electrode are gradually consumed, and the pH of the anolyte is increased to reduce the reduction electrode potential and restrict the movement of the electrons.

Therefore, it is necessary to provide a condition that suppresses the transfer of cations through the ion exchange membrane and facilitates the transfer of hydrogen ions. For this purpose, an alternative is to use a catholyte having a low concentration of the cation as much as possible, or a thin ion exchange membrane, which is a medium through which hydrogen ions are transferred to the reducing electrode. In addition, the need for the development of microbial fuel cells without using ion exchange membranes has emerged.

1.1.2. Photosynthetic microbial fuel cells

Photosynthetic microbial fuel cells are a type of MFC. [3, 17]. Conventional MFCs oxidize the supplied organic fuels and transfer electrons to the electrodes. The transferred electrons are reduced at the cathode to produce electric power. On the other hand, photosynthetic MFCs produce electrons by the photosynthesis reaction of algae cells without supplying organic fuel. As a result, it is possible to produce electric power using only solar energy without external energy supply. During the photosynthesis process, high energy electrons are produced in the algae cells. These electrons can be extracted out using an electrically conductive pili, electron redox mediator.

1.1.3. Direct extraction of photosynthetic electrons from algal cells

With advances in micromachining technology, many microtip-type electrodes have been realized using three-dimensional techniques for the fabrication of micrometer-scale structures. The microtip electrodes are particularly attractive because of their sharpened features. These microtip electrodes have a wide variety of applications, such as field emission displays, scanning tunneling microscopy, scanning electrochemical microscopy, and various biological applications [18].

Microfluidic chips are used in a wide variety of applications in biology, medicine, and chemistry as micro-electro-mechanical systems (MEMS) technology advances [19, 20]. Among them, PDMS microfluidic chips are most widely used in lab-on-chip research due to their advantages such as low cost, simplicity, speedy

process and biochemical stability. When electrodes are arranged in the flow path of the microfluidic chip, it is possible to classify and analyze target materials injected in the flow path by using electrophoresis and dielectric electrophoresis through electrical signal application. And it can be used as a sensor because it can detect specific elements through electrochemical measurement.

The reaction of thylacoid in the chloroplast during photosynthesis is shown in the Figure 1-2. When sunlight stimulates PS2, it produces electricity by electrolyzing water. The produced electrons are transferred to PS1 through electron transfer proteins such as plastoquinone, cytochrome, and plastocyanin. The electrons transferred through ferredoxin in PS1 convert NADP to NADPH by FNR enzyme and contribute to cell metabolism.

It is possible to extract electrons from the ferredoxin of the chloroplast thylakoid membrane to the outside of the cell by inserting the electrode into the cell using microfluidic chip and micro probe production technology.

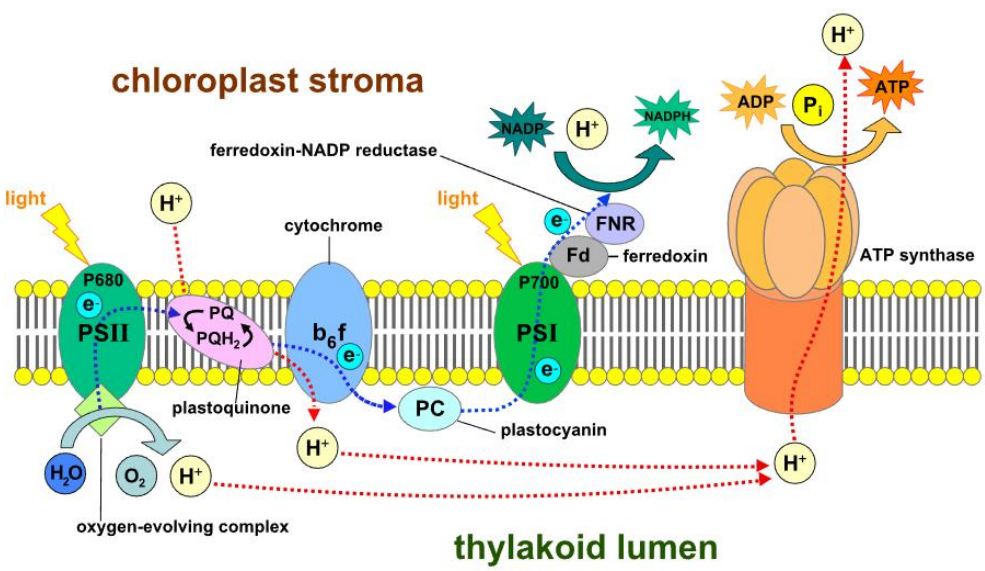

Figure 1-2. Light dependent process during photosynthesis [21].

1.2. Motivations and objectives

1.2.1. Motivations

For most types of PMFC, since photosynthesis occurs inside chloroplasts, high-energy electrons are not accessible to external electrodes. As a result, exogeneous electron mediators are needed to transfer photosynthetic electrons to electrodes; however, most of the mediators are toxic, which limits the lifetime of the PMFC.

To overcome this limitation, several novel designs have been proposed and explored [22-26]. For example, polymer-coated electrocatalytic electrodes facilitate the electron transfer between photosystems and electrodes. Another approach to circumvent the problem is to utilize subcellular plant photosystems [27]. Thylakoids are isolated after grinding spinach chloroplasts, and then chlorophylls in a suspension transfer electrons directly to an anode. However, this requires a tremendous amount of effort for cell preparation, and is not self-sustainable.

One way to overcome this complexity is to place an electrode into the cytosolic space of a cell. By locating a nanoelectrode inside a living C. reinhardtii cell, high-energy electrons generated during photosynthesis were extracted directly without a mediator [28]. This demonstrated that high-energy photosynthetic electrons could be harvested from photosynthesis-related proteins, such as cytochromes or ferredoxins. However, since the amount of electrons produced during the photosynthesis of a single cell is extremely small, the current was of the order of pico-amperes. Therefore, scale-up of this approach is required in order to use this electron harvesting method to fabricate a PMFC.

1.2.2. Research objectives

This dissertation aims to develop a through-polydimethylsiloxane microtip electrode array that can be applied to photosynthetic fuel cells. Previous studies used a method of inserting an electrode into a algal cell to extract current. In order to overcome a low efficiency power extraction which is the drawback of this method, we aimed to extract power from the single layer stacked cell array using microtip electrode and microfluidic device fabrication technique. In order to achieve this, a method of inserting a microtip electrode array into an algal cell stacked in a microfluidic device has been proposed.

The microtip electrodes are fabricated through a combination of the silicon anisotropic/isotropic etching process. Through deposition/etching of conducting layer and insulating layer, the electrodes are formed at the end of the microtip. The performance of the electrode is verified through electrochemical measurements. Photosynthesis algae cells are assembled with microfluidic devices by inserting microtip electrodes into the PDMS microfluidic device. The sharp end of the fabricated microtip electrodes are located within the channel by penetrating the bottom thin film of the PDMS channel.

In the experimental part, the short-circuit current and the open-circuit voltage are measured to verify the use of the microbial fuel cell. Also, based on the analysis of the loss of the measured results, we propose a method to reduce the current loss through the improvement of the electrode arrangement and the microchannel structure.

1.3. Dissertation organization

This paper contains two main contents. The first is the intracellular inserting method of the electrode using the through-PDMS insertion method, and the second is the development of the micro-probe electrode array having the conductive end of the electrode.

The composition of the paper is as follows. Through-PDMS insertion method is introduced and the design process is explained. Photosynthetic algal cells are combined with microfluidic devices by inserting microprobe electrodes into PDMS fluidic devices. The sharp tip of the fabricated microprobe electrode is located in the channel by penetrating the lower layer of the PDMS fluid channel.

Next, fabrication of conductive microtip array is introduced with explanation of a combination of silicon anisotropy / isotropic etching processes. The aspect ratio of the silicon microtip and the tip radius are controlled by a mask design that changes the diameter and spacing of the etch mask pattern. Through electrochemical measurements, the performance of the electrodes was verified and compared with the evaluation based on the conical microelectrode theory.

Next, a method of measuring the short circuit current and the open circuit voltage of the inserted electrode array is described. The used cell and the experimental environment are also described. The measured results are analyzed using current loss analysis through electrochemical simulation and effective electrode calculation. A design is proposed to avoid losses through the analyzed results.

Chapter 2. Through-PDMS insertion method

2.1. Introduction

With the development of micro-electro-mechanical systems (MEMS) technology, microfluidic devices have been used in a broad range of applications in biology, medicine and chemistry [29, 30]. Above all, microfluidic devices made of polydimethylsiloxane (PDMS) are the most widely used in lab-on-chip research because of the advantages of low price, rapid process, and biochemical stability [31, 32]. In the above applications, it is essential that microfluidic chip includes sampling and sensing parts of target materials.

The sampling part stands for a designed structure that target particles/molecules are immobilized in the microfluidic channel before the sensing process. The structures such as dam, weir and pillars in the microfluidic channel have been reported for trapping particles in a particular region [33-35]. If the trapped particles are densely packed in the channel, the sensing signal could be enlarged with increased particle numbers [36-38].

In the case of electrochemical applications, sensing part is composed of microelectrodes. When the microelectrode is placed in the channel of these microfluidic chips, the target material injected into the channel can be classified and analyzed by using electrophoresis and dielectric electrophoresis phenomena through electrical signal addressing [39, 40]. Moreover, it can also be used as a sensor because a particular molecule can be detected through amperometric, voltammetric or impedimetric electrochemical measurements [41, 42].

In addition to these problems, if densely and complexly designed electrodes

need to be placed in the channel, it is not easy to place electrodes as desired because of the limit that the electrodes are formed on a two-dimensional plane. Complex integration of electrodes also causes unstable sensing due to high parasitic capacitance and interference of signal between electrodes.

In the case of an integrated platform that includes packing particles and electrical sensing, PDMS channel with electrodes is usually formed by bonding or placing molded PDMS on the electrode patterned on the glass substrate and signal is applied from the outside. However, PDMS and the metal electrode surface are not permanently bonded using existing methods. If the pressure injecting a fluid is increasing in incomplete bonding, a fluid leaks out through unbonded electrode surface, affecting experimental reliability and consistency. To prevent this problem, several bonding techniques between the PDMS mold and the electrode are attempted using adhesive materials such as polymer epoxy, photoresist and uncured PDMS on the electrode connection part [43]. However, there are the disadvantages of expensive price and additional manual process, respectively.

For through-PDMS insertion method, an electrode arrangement in the microfluidic device using inserting the silicon-based electrode in the PDMS fluidic channel is proposed. This method is realized by penetrating the bottom thin film of the PDMS fluidic channel with sharp end of the electrode. For easy penetration, the electrode was fabricated in the form of sharp microtip and designed to be positioned in the channel by fabricating arrangement layer around the microtip electrode. Using the proposed method, it is possible to address the electrode lines in a vertical direction from out of the microfluidic device. Because the material of microtip is silicon, the microtip electrode can recycled after inserting/extracting process.

2.2. Design of through-PDMS insertion method

2.2.1. Design of assembly process

Figure 2-1 shows a schematic view of the proposed device. This device consists of a microtip electrode array and a microfluidic channel. Each part is manufactured separately and then assembled using vertical alignment. Microtip electrode array was designed to be located in the center of the channel for precise positioning to planar and vertical direction. Using alignment layer formed around microtip, location of the bottom surface of PDMS thin film is controlled by the inserting end of the microtip in the channel. The substrate of microtip electrode is silicon that has strong mechanical stiffness.

While the thickness of the top plate of the fluidic chip is several millimeters like common PDMS fluidic chip, the bottom surface was designed so that the microtip electrode can pass through a thin film and be inserted into the channel. The thickness of PDMS thin film is designed as 20 μm, which is capable thickness for being penetrated by microtip electrode. The height and width of the channel are 10 μm and 4 mm, respectively. To prevent upward bending of the PDMS membrane during assembly process, 100-μm-width PDMS cylindrical pillars are designed in 100 μm gap.

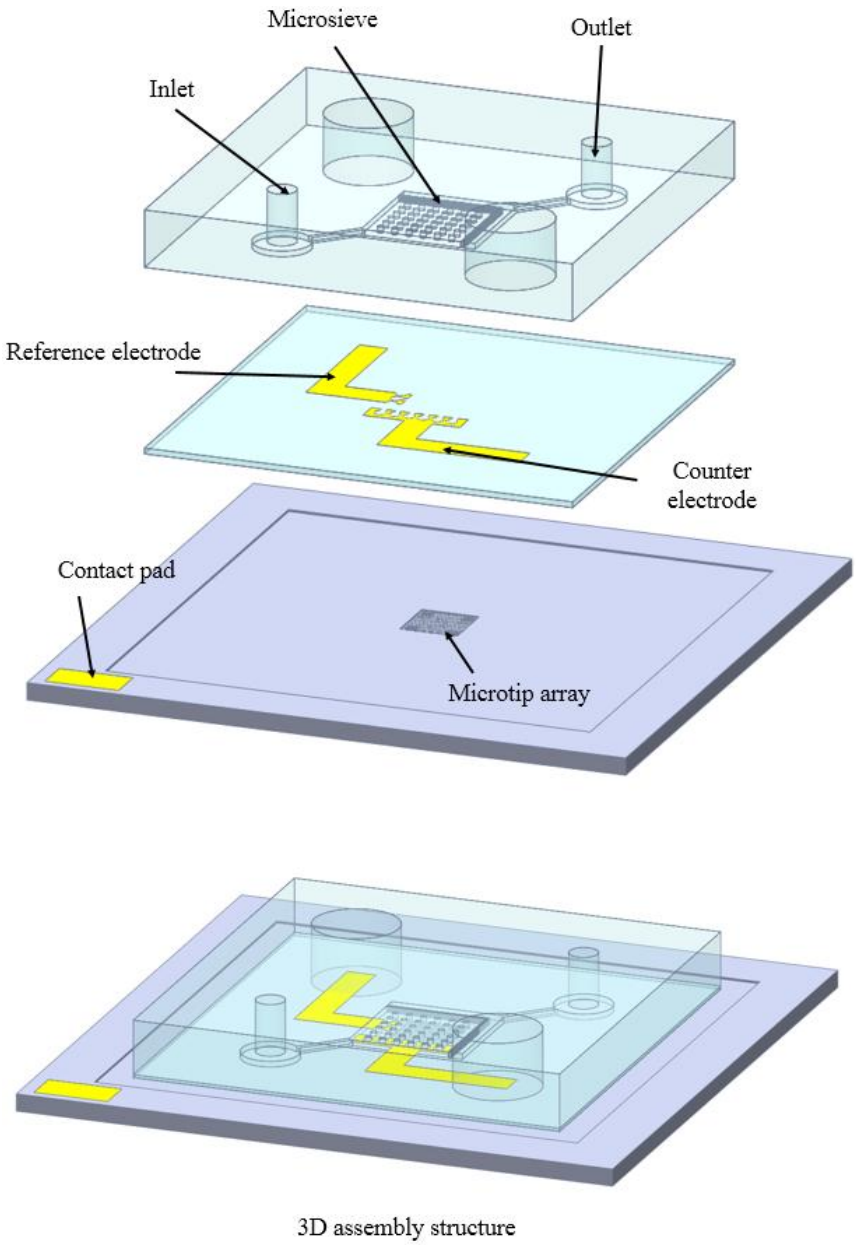

Figure 2-1. Schematic view of the proposed device.

2.2.2. Design of conductive microtip

A design parameters of microtip electrode array is shown in Figure 2-3. The cells used in this study are spherical cyanobacterial cells. The cells are arranged in a single layer within the microfluidic chamber. In order for electrodes to be inserted

into a single layer of algae cells, the aspect ratio of the electrodes should be high and the radius of the tip of the microtip should be several tens of nanometers. And the width of the exposed electrode should be small enough to measure current in the cell. In this paper, the electrode is designed to be less than 1 μm × 1 μm to facilitate the measurement of current in the cell. A localized UME is formed at the end of the microtip by depositing and patterning the insulating layer without an additional photolithography step.

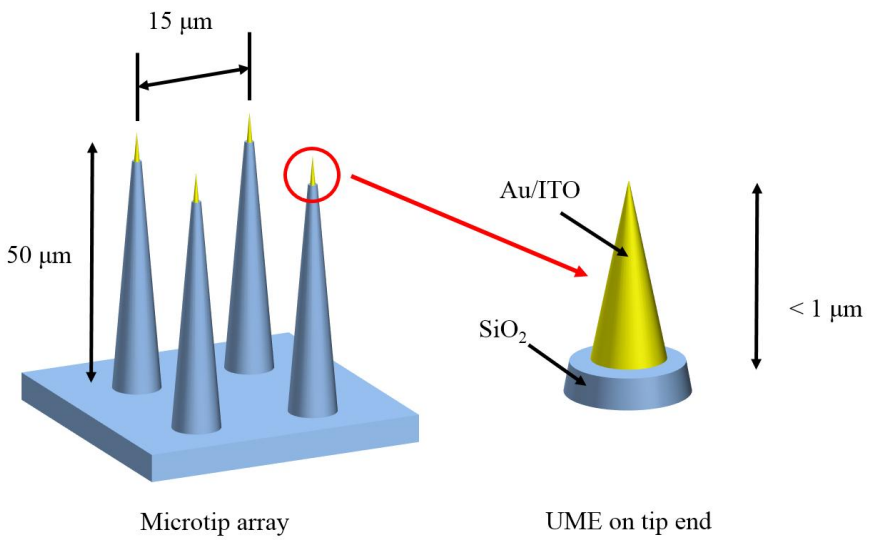

Figure 2-2. Design parameters of microtip electrode arary

For electrical connection, the end of the microtip is exposed as the electrode, and the remaining area is insulated with silicon oxide layer. The height of the microtip was designed to be about 50 μm and the distance between the microtips is 15 μm.

The PDMS thin film is determined according to the spin coating rate in the process. The thickness of the thin film is an important factor when the electrode is inserted into the chamber. When the thickness of the PDMS thin film is thick, the

rigidity of the thin film is increased. However, the possibility of touching the ceiling is high due to the frictional force with the electrode. In this paper, the thickness of the thin film was determined to be 20 μm, which is the minimum thickness that can be fabricated.

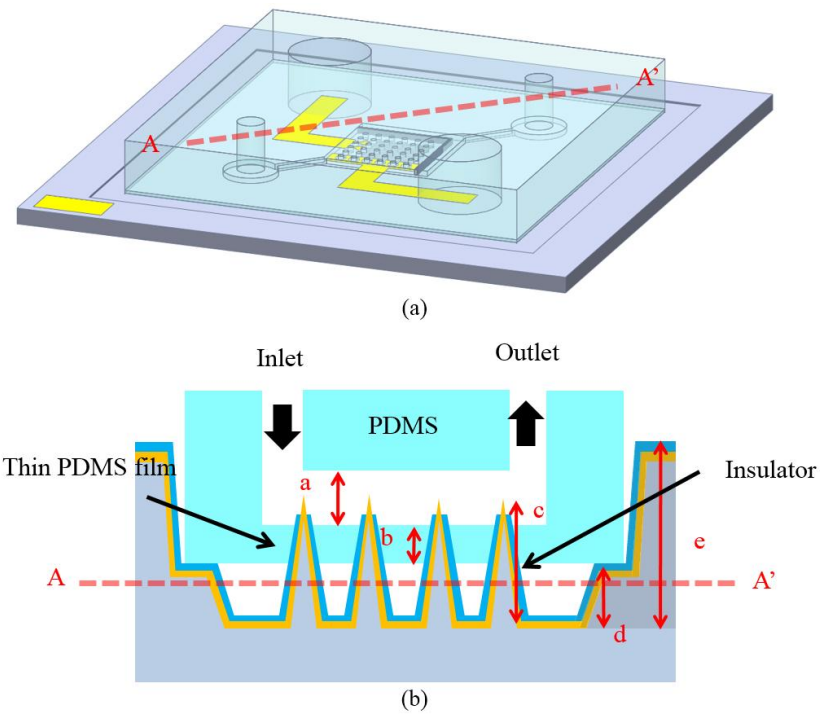

Figure 2-3. Detailed design parameters of the proposed device.

The alignment layer contacts the bottom of the PDMS chamber as shown in the Figure 2-3 to position the end of the electrode in the PDMS chamber. As a result, the height of the microtip electrode is determined by adding the height of the chamber and the height of the PDMS film to the height of the alignment layer. In this paper, the value of the microtip electrode was determined as 45 ~ 55 μm as shown in the Table 2-1.

$$h_{align} + h_{chamber} + h_{film} = h_{microtip} \qquad (2\text{-}1)$$

Table 2-1. Designed parameters and target dimension

	Parameter	Target dimension
a	Height of fluidic channel	~ 10 μm
b	Thickness of PDMS film	~ 20 μm
c	Height of microtip	~ 50 μm
d	Height of alignment layer	~ 25 μm (20 ~30 μm)
e	Height of silicon frame	~ 70 μm

2.2.3. Design of microfluidic chamber

The microfluidic chamber was designed to arrange cells into a single layer. To immobilize the cells, a microsieve should be designed and prevented from flowing into the outlet. In this paper, a microsieve having a width of 3 μm, which is smaller than 10 μm, was prepared in a microfluidic chamber to fix the cells since cyanobacterial cells have elastic cell walls

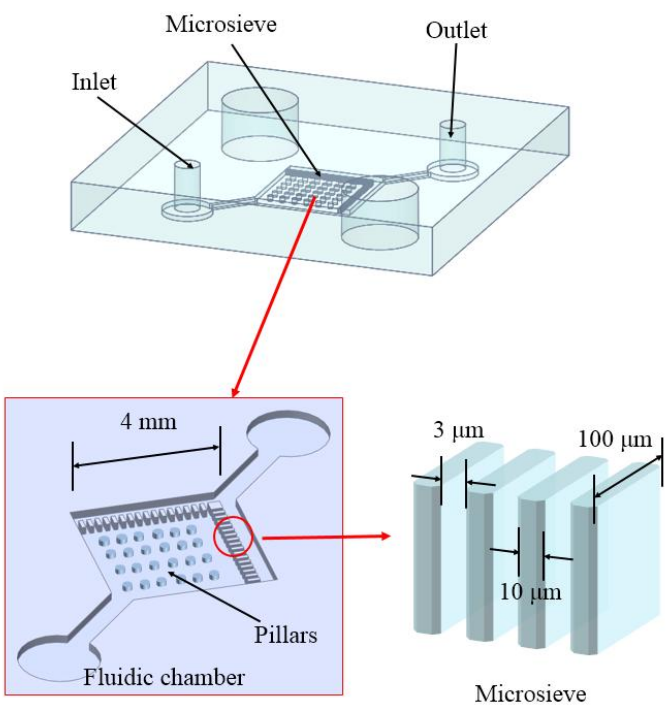

Figure 2-4. Design parameters of microfluidic chamber

A microfluidic channel that the electrochemical measurement is possible after assembling with microtip array was designed with metal electrodes. For the electrochemical measurement of cell analysis, working/counter/reference electrodes should exist, and each electrode has to be connected to the outside. In our proposed structure, microtip electrode array plays a role of working electrode and the electrode manufactured within a chamber plays roles of counter and reference electrodes.

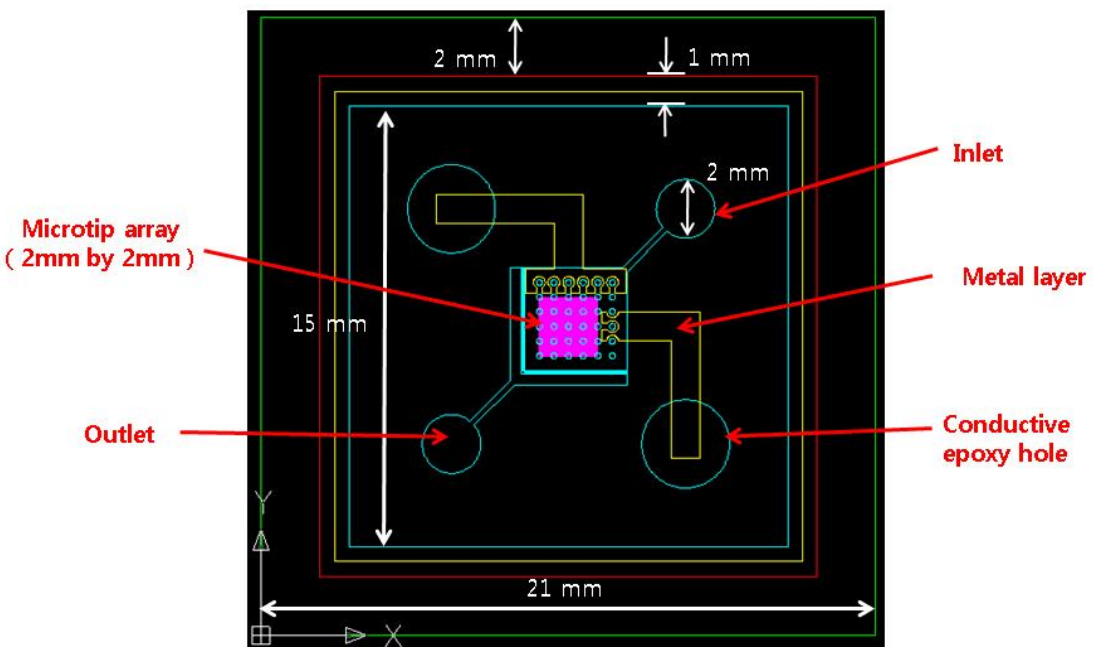

Figure 2-5. Mask layout of microfluidic device.

As the Figure 2-5, the entire size of single tip array and multiple tip array samples was designed as 21 mm × 21 mm. With considering misalignment and manipulation, the size of the microfluidic chip was decided as 15 mm × 15 mm. The metal electrode patterned using shadow mask is connected to the outside through a hole filled with conductive epoxy.

As shown in the Figure 2-6, a working electrode, a counter electrode, and a

reference electrode are arranged in the chamber. The microtip electrode array is placed in the center, and the counter electrode is arranged at a size of 3.4 mm × 0.8 mm on the one side of the channel. A cylindrical pillar was placed in the chamber to prevent the PDMS film from reaching the ceiling. The diameter of the pillar was 100 μm and the spacing between the pillars was designed to be 100 μm.

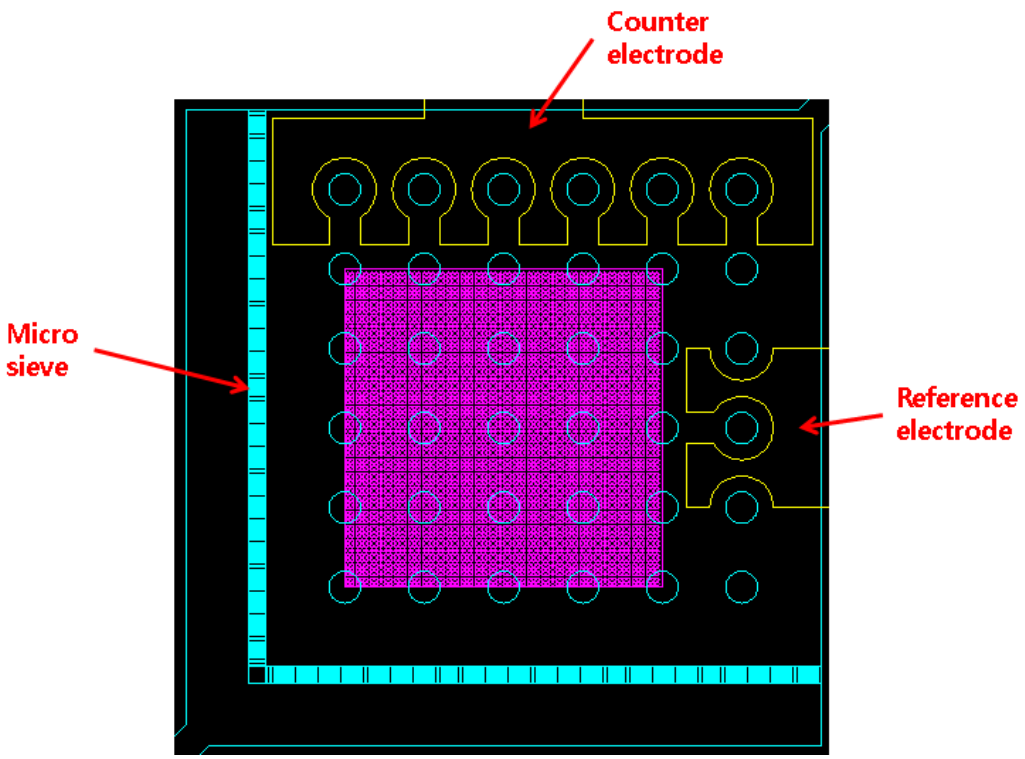

Figure 2-6. Electrode arrangement in the chamber.

2.3. Fabrication process

A microtip electrode is manufactured by the method of depositing the electrode and insulating layer on silicon microtip array based on silicon and then etching only the end of the microtip. Figure 2-7 shows the process of a microtip array electrode. First, a silicon substrate is vertically etched by using oxide-film mask (Figure 2-7(a)) and then a silicon column is shaped into a silicon microtip through the isotropic etching process by using SF_6 gas (Figure 2-7(b)). Then, to form the arrangement end to determine the position of the microtip in the channel when boning combined with a microfluidic channel device (Figure 2-7(c)). After silicon microtip array is manufactured by forming the arrangement end, ITO and SiO_2 acting as electrodes are deposited (Figure 2-7(d)). Next, the manufacture of the microtip electrode array is completed by applying a sensitive film to the front of the substrate and etching the oxide film of the end of the microtip and then removing a sensitive film (Figure 2-7(e)).

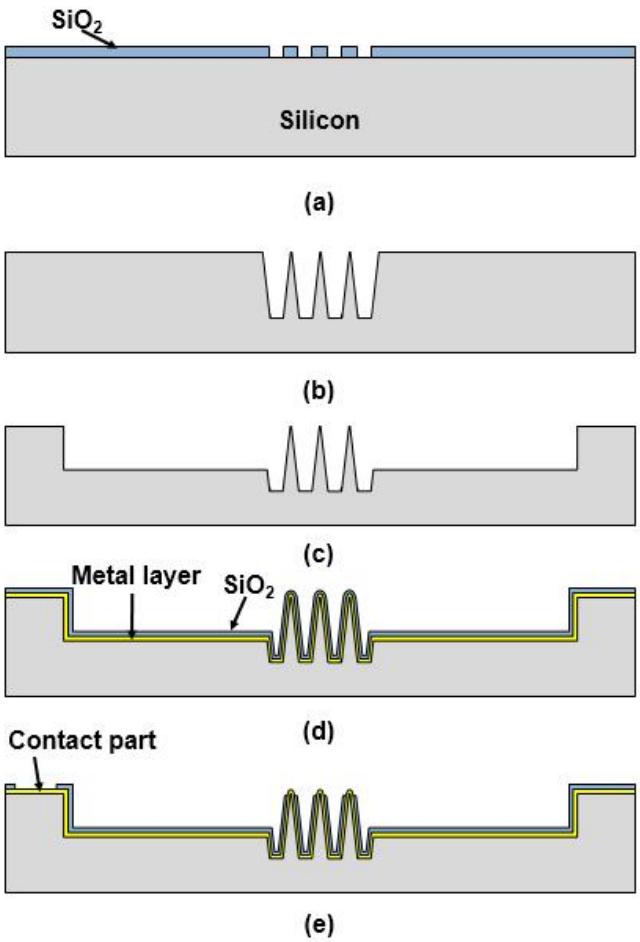

Figure 2-7. Fabrication process

Figure 2-8 shows a process flow of a PDMS microfluidic chip fabricated by soft lithography technology involving following three steps: (1) PDMS replica fabrication; (2) Electrode formation on PDMS thin film; (3) Bonding PDMS replica and thin film.

First, silicon master was etched using DRIE step with channel height and fluorocarbon polymer was deposited for easy detachment of PDMS from silicon master (Figure 2-8(a)). PDMS pre-polymer mixture (10:1) was poured on the silicon master and cured for 3 hours at 70 °C. After the curing process was completed, a PDMS replica was peeled off from the master. The injection holes

were punched through PDMS replica (Figure 2-8(b)).

The electrode formation steps were processed using glass substrate fluorocarbon polymer deposition. On the glass substrate, PDMS pre-polymer mixture was spin coated at 3000 rpm for 40 s to control the thickness of PDMS film. In order to deposit reference electrode, Ag was sputtered on PDMS film with 5000 Å. In the case of counter electrode, Cr/Pt was sputtered with 500/5000 Å. These electrodes were patterned using stencil method with silicon shadow mask.

The fabricated PDMS replica was bonded to PDMS thin film using hydroxyl group treatment. Both PDMS are exposed to surface treatment which generates hydroxyl groups on the PDMS. For this treatment, a corona discharge method is used at PDMS replica for 2 min by handheld high frequency generator (BD-10A, Electro-technic products, inc.) with voltage of 50 kV. However, since metal layer can be attacked by corona discharge, PDMS film on slide glass is treated in O_2 plasma chamber for 2 min. Since bonding adhesion between PDMS and metal is poor, PDMS replica and film were aligned in order to minimize contact area between PDMS replica and metal electrodes on the PDMS film.

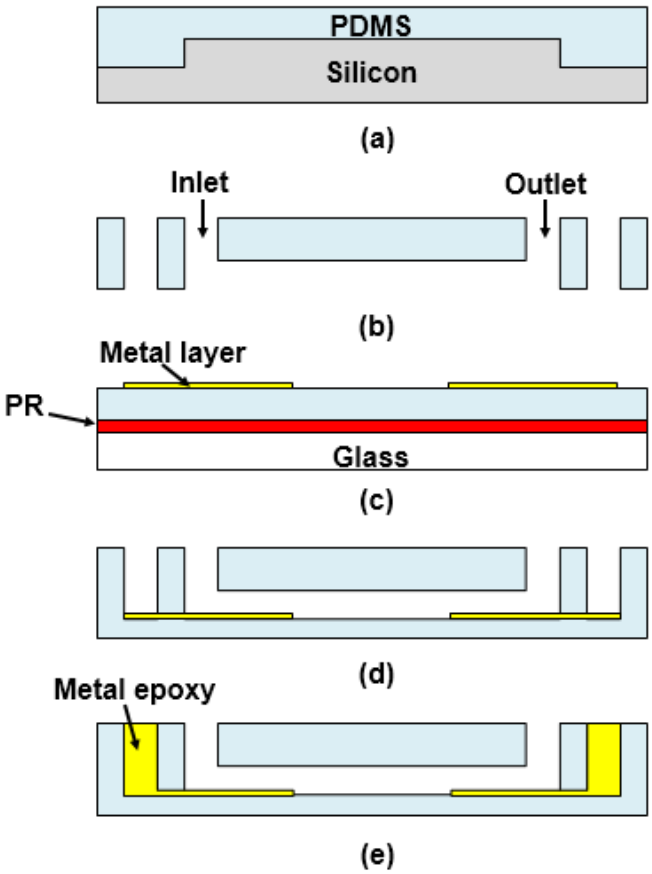

Figure 2-8. Fabrication process of PDMS fluidic device.

2.4. Assembly process

A schematic of assembly process is shown in Figure 2-9. The fabricated microtip array vertically penetrates the PDMS membrane and consequently the exposed electrode on the microtip is located in microfluidic channel so that electrode can measure the electrical signal in the channel after the assembly process. A design considerations in the assembly process is that horizontal movement of devices during vertical assembly should be maximally restricted. When the microtip array moves horizontally in the assembly process, there is a disadvantage that it can be broken easily by the horizontal force as the width of the microtip is only a few micrometers. Moreover, PDMS membrane that has a thickness of several tens of micrometers is also expanded by the horizontal force.

To reduce the movement in the horizontal direction and apply a constant force in the vertical direction, we design an acrylic jig as shown in Figure 2-9. The acryl jig consists of three acryl plates, micrometers and springs. Each of the top and bottom plates is attached with micrometers in fixed condition and the distance between both plates is controlled using micrometers. With the controlled distance, a constant repulsive force is applied to the microtip array and microfluidic chip due to the spring between the bottom and middle plates. To minimize horizontal and axial movements, four metal bars with ball bearings are mounted through three plates.

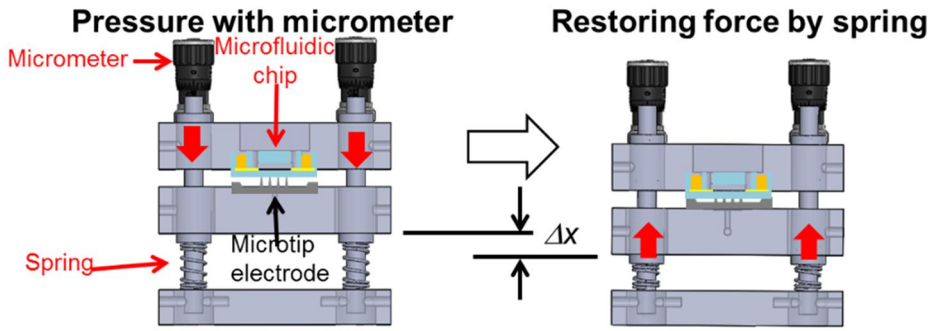

Figure 2-9. The acryl jig consists of three acryl plates, micrometers and springs

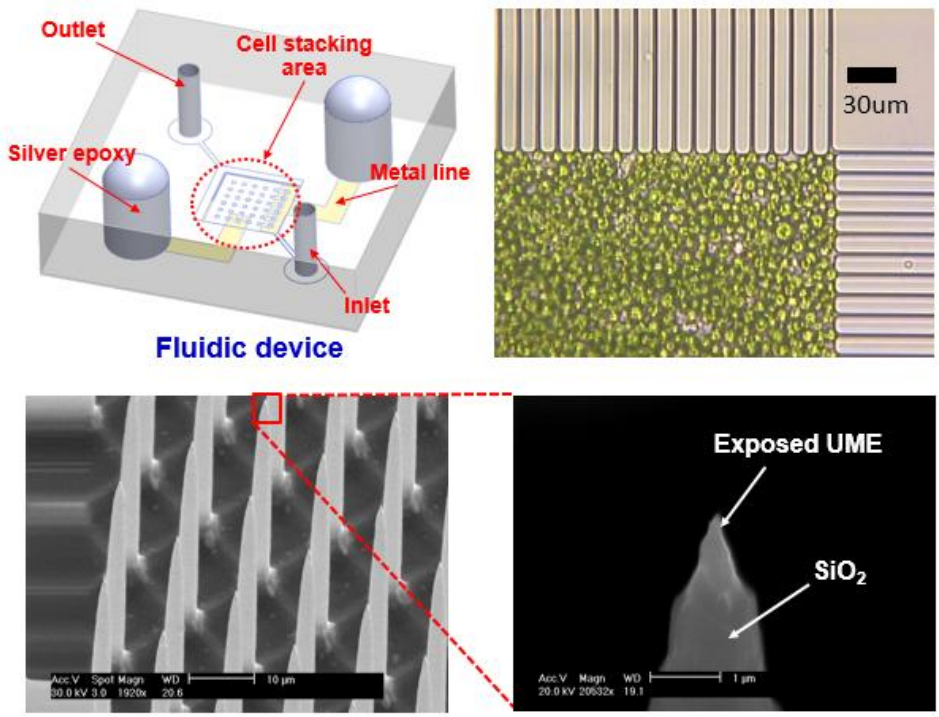

Figure 2-10. Fabricated fluidic device and silicon microtip.

Chapter 3. Fabrication of conductive microtip electrode

3.1. Introduction

With advances in micromachining technology, many microtip-type electrodes have been realized using three-dimensional techniques for the fabrication of micrometer-scale structures. The microtip electrodes are particularly attractive because of their sharpened features. These microtip electrodes have a wide variety of applications, such as field emission displays, scanning tunneling microscopy, scanning electrochemical microscopy, and various biological applications [18].

In biological application, which is one of the purposes of microtip electrode research, the sharpened features of the microtip electrode are used for penetrating tissues or cell membranes to sense electrical signals from target organisms, or to transmit signals to them. In neuroscience, microtip electrodes are used to penetrate the cell membrane, and to sense more critical electrical information than with non-invasive methods [44]. Also, microtip electrodes can extract electrons produced in vegetable cells by the photosynthetic reaction. Due to the electrically conductive tip end with an insulation layer, the electrodes can be used as an anode electrode for photosynthetic electrochemical fuel cells in a target cell [45].

Generally, the aspect ratio of the microtip and the sharpness of the end of the tip are important specifications. In terms of controlling these specifications, silicon is an appropriate material due to its relatively well-established etching techniques. Furthermore, its high mechanical stiffness and chemical resistance are considered advantages for use in electrodes or substrate structures.

The shape of a silicon microtip electrode is determined by its fabrication method. To realize the vertical shape of a microtip with a high aspect ratio, most have used bulk micromachining technology on silicon substrate, or surface micromachining with deposition of a thin-film layer as a microtip structure [46-48]. One simple method to fabricate a silicon microtip is anisotropic wet etching using different etch rates that vary with the crystal orientation of silicon [48]. This method is efficient for fabricating silicon microtips due to its single etching process. However, the shape of a microtip is limited, because the silicon etch rate is fixed according to the crystal orientation. Dual etching processes are alternative to solve problems with monotonous shape. A combination of anisotropic and isotropic etching is appropriate for fabricating diversiform and high-aspect-ratio silicon structures. Deep reactive ion etching (DRIE) is a representative anisotropic etching method for silicon. Y. Hanein et al. demonstrated that the combination of DRIE and reactive ion etching (RIE) can be used to fabricate a silicon needle with a height of more than several hundred micrometers [47]. N. A. Aziz et al. used a dicing process to form vertical silicon square pillars, followed by the HNA isotropic wet etching of silicon to obtain a sharp tip end [46].

For sensing an electrical signal from a specific area in an organism, the conductive part of a microtip electrode should be placed at the end of the microtip, and the other areas should be electrically insulated. The conductive area should also be fabricated to be narrower than the diameter of the target tissue or cell. The fabrication of the conductive part on a high-aspect-ratio structure has been introduced [49]. However, there have been few studies on fabricating high-aspect-ratio microtips and the formation of a UME with a conductive area of less than one micrometer.

For through-PDMS insertion method, this chapter presents the detailed analysis and verification of the fabrication results of a conductive microtip array with localized UMEs at the tip end, based on the concept of microtip fabrication introduced in our previous work [50]. In order to use a microtip electrode in penetrating applications, a study on the variation of electrode design is necessary. A silicon microtip is fabricated using a combination of DRIE and sulfur hexafluoride (SF_6) RIE steps. The shape of the microtip is transformed from pillar type to tip type by the variation of the sidewall etching rate of the pillar in the SF_6 RIE step. The aspect ratio and the apex radius of the silicon microtip are controlled by mask design with varying diameter and gap of etching mask patterns. A detailed investigation of the proposed fabrication process and the etching behavior according to the relation between the mask geometry and the shape of the microtip is discussed in this chapter. A localized UME is formed at the end of the microtip by depositing and patterning the insulating layer without an additional photolithography step. After the fabrication, electrochemical characterization of the UME was performed using cyclic voltammetry (CV), and compared with an estimation based on conical UME theory.

3.2. Microtip formation mechanism

A schematic view of the microtip formation mechanism is shown in Figure 3-1. The figure shows the transformation process from the cylindrical silicon pillar into the microtip structure during the isotropic etch process. At first, through the anisotropic etch process, the cylindrical pillar structure is formed along the vertical direction with etch mask material on the top. During the isotropic etch step, the etch rates at the vertical sidewall of the cylindrical pillars are varied depending on the position at the sidewall.

The etch rate difference originates from the etching mechanism of RIE. In the RIE process, the chemical etching and the ion-enhanced etching are two main mechanisms that simultaneously affect the etch rate and the shape of the etched material. Depending on the process temperature, neutral radicals in the plasma contribute to the chemical and isotropic etching of silicon, while ion enhancement by bias voltage is involved in anisotropic etching according to the ion energy and ion distribution angle. In the RIE process after the formation of a high-aspect-ratio structure, the radical delivery by the flow of etching gas slows down at a deeper depth, and the ion angle distribution is shadowed by mask material on the top of the structure [51]. Therefore, the shape of the cylindrical pillar transforms into an hourglass-shaped pillar. These tendencies appear differently in the etched shape of the cylindrical pillar with a varied gap between the circular etch mask patterns. As depicted in Figure 3-1, with a narrow gap between masks, the radical delivery and ion distribution angle at a deeper depth are limited by the narrow width of the cavity. Consequently, a high-aspect-ratio microtip structure can be formed, because the etch rate at the top side of the pillar is higher than that of the bottom side.

Circular etch mask arrays with a varying diameter and gap between patterns are used for the fabrication of microtip arrays with different aspect ratios and shapes. The diameter was varied from 20 μm to 50 μm, and the gap between the mask patterns was varied from 10 μm to 50 μm in a different array.

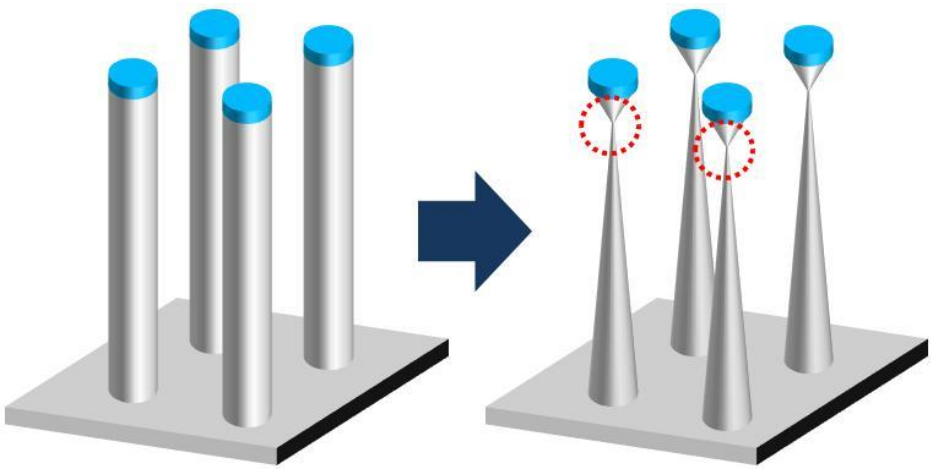

Figure 3-1. Schematic view of the microtip formation mechanism

3.3. Fabrication process

The proposed fabrication method consists of two main steps with a single photolithography mask. The first step is the formation of the silicon microtip, which acts as a substrate structure for the electrode. The second step is UME fabrication on the silicon microtip. The first step involves anisotropic and isotropic dry etch processes, using the Bosch process and RIE with SF_6 gas, respectively. In the second step, the silicon microtips are successively coated with conducting and insulation layers, followed by the patterning process of the insulation layer to form an UME at the tip end.

The detailed fabrication steps are shown in Figure 3-2. A 525-μm-thick, 10-mm-diameter, p-type (100) single-crystalline silicon wafer is used as a substrate for the silicon microtip structure. The first step was the deposition of a 1-μm-thick layer of silicon dioxide, which would be used as a hard mask in the following dry etch steps. This hard mask was deposited on silicon substrate by chemical vapor deposition (CVD) and patterned using RIE equipment (P-5000, AMK). The silicon substrate was then vertically etched about 50 μm by DRIE with the conditions summarized in

Table 3-1

Table 3-1. After forming the silicon pillar, the photoresist on the SiO_2 was removed by an oxygen (O_2) plasma asher (V15-G, Plasma finish). Typically in the DRIE process, a polymer is deposited on the sidewall of the silicon pillar, and a residue remains after the process. To remove the residue, the sidewall of the silicon pillar was wet etched slightly using 29 wt% concentrated potassium hydroxide

(KOH) solution at 75°C.

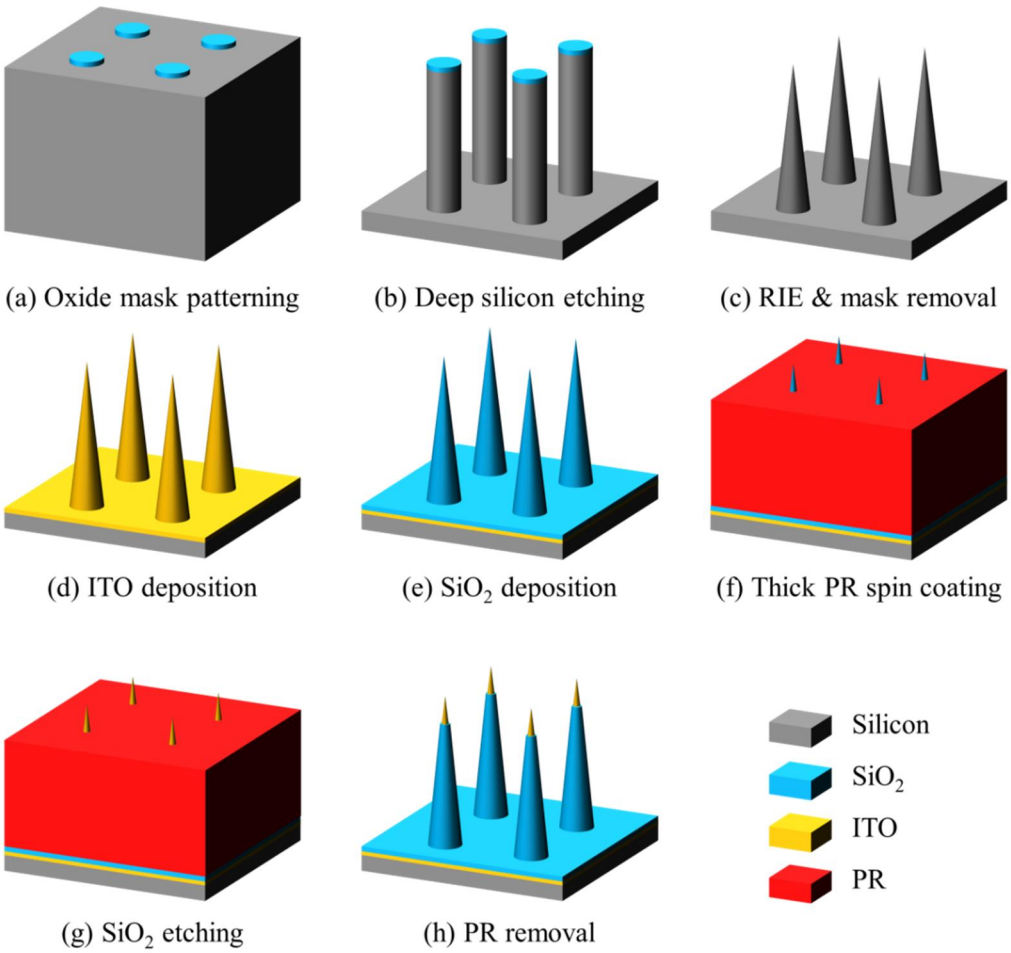

Figure 3-2. Fabrication steps of microtip electrode

The vertically fabricated silicon pillar was then etched by RIE in an inductively coupled plasma (ICP) etcher (SLR-880-10R-B, Oerlikon). The RIE process was conducted with the same conditions of the silicon etch step of the DRIE process. In this process, the cylindrical silicon pillar was transformed into an hourglass shape with a narrow center, the diameter of which was continuously reduced. The top part of the hourglass-shaped silicon pillar was removed from the body after an appropriate etch time, and it was clearly removed from the wafer in

the cleaning step using the Piranha solution (4:1 mixture of 98% H_2SO_4 and 30% H_2O_2). After removing the SiO_2 hard mask in the outer area of the microtip array using 49% concentrated hydrofluoric acid (HF) solution, the first part of the main steps was completed.

Table 3-1. Etching conditions for DRIE process

	Coil power (W)	Pressure (mTorr)	Time (s)	Gas flow (sccm)	
Step 1 : Polymer deposition	825	22	5	C4F8	100
				SF6	0.5
				Ar	30
Step 2 : Polymer etch	825	23	3	C4F8	0.5
				SF6	50
				Ar	30
Step 3 : Silicon etch	825	23	5	C4F8	0.5
				SF6	100
				Ar	30

In the second part, the UME was realized by opening the metal area at the tip end. 2000 Å /1000 Å of gold/indium tin oxide (ITO) layer was deposited as a conducting layer on the fabricated silicon microtip by metal sputtering (SPS4150, Ultech). The silicon dioxide layer was also deposited as an insulating layer using the CVD process. After completing the deposition steps, the wafer with the microtip structure was cut by a dicing saw (DAD 522, Disco) in order to carry out remaining steps at the chip level. Next, for patterning the SiO_2 layer at only the tip end, viscous photoresist (AZ4620, Clariant) was spin-coated to form a layer with a

thickness of 25 μm. The microtip coated with conducting and insulating layers was entirely covered with thick photoresist in the spin coating process, but the thickness of the photoresist at the tip end was very thin due to the high aspect ratio and sharp shape of the microtip structure. In the next step, the whole area of the chip was etched in an RIE etcher (Plasmalab 80 Plus, Oxford Instrument) with a gas mixture of carbon tetrafluoride (CF_4) and O_2 at 55 mtorr for 15 min, without an additional photolithography process. The selectivity ratio, which is the proportion between the etch rate of the SiO_2 and that of the photoresist, was set to about one in order to etch the two materials simultaneously in one step. In this etching process with a low selectivity ratio, the thin photoresist on the tip end is removed first, and then the SiO_2 layer is etched until the conducting layer is exposed at only the tip end. Finally, the fabrication of microtip electrode is completed with the removal of the photoresist by dipping into AZ700 photoresist remover (Clariant) at 120 °C. The Table 3-2 shows the sequence of detailed fabrication processes.

Table 3-2. Sequence of detailed fabrication processes.

Step	Fabrication	Machine	Detailed condition
10	SPM cleaning	Wet station	Piranha solution, 10 min
20	SiO_2 deposition	P-5000 CVD	1 μm thickness
30	Photolithography	MA6-2	AZ1512, 1.2 μm thickness
40	SiO_2 etching	P-5000 Etch	20% over etching
50	PR removal	Asher	10 min
60	PR removal	Wet station	Piranha solution, 10 min

70	Deep silicon etch	DRIE etcher	50 μm depth
80	Polymer removal	Wet station	40wt.% KOH, 45 sec
90	SF6 RIE	DRIE etcher	3~4 min
100	SiO_2 removal	Wet station	HF, 1 min
110	SPM cleaning	Wet station	Piranha solution, 10 min
120	Au/ITO deposition	Sputter	2000 Å /1000 Å
130	SiO_2 deposition	P-5000 CVD	3000 Å thickness
140	PR spin coating	Spin coater	AZ4620, 21 μm thickness
150	PR hard baking	Hot plate	115˚C, 30 min
160	SiO_2 etching	Oxford 80+ etcher	150 W, 20 min
170	PR removal	Wet station	AZ700 remover, 120˚C

3.4. Fabrication results

In this section, the results of fabrication and the etching characterization of silicon pillars are discussed, considering differences in diameter, the gap between patterns, and the etching time. After the DRIE and KOH wet etching process, the width of the vertical silicon pillar is reduced by about 3 μm from its designed value. In the subsequent RIE process, the shapes of the etched silicon pillars differ when varying the gap between pillars. Figure 3-3 shows the etching profile of silicon pillar sidewalls with different etching mask gaps according to the RIE etching time. The differences in the etch rate at the sidewall can be characterized by measuring the width of the hourglass-shaped pillar in the side view scanning electron microscope (SEM) image. As the etching time increases, the silicon pillar is etched in the vertical and horizontal directions, and the fastest etched part in the horizontal direction becomes the end of the microtip. The height of the microtip is determined by the gap between etching masks. As shown in Figure 3-5(d) and (e), the fabricated microtips with the etching mask gaps of 40 μm and 50 μm have low aspect ratios, because the wide gaps between the SiO_2 mask patterns induce a higher etch rate at the bottom of the silicon pillar compared to the top. If the gap is 10 μm, the etch rate of the top side is greater than that of the bottom side. In the case of 20 μm and 30 μm gaps, the etch rates of the top and bottom are similar, so the microtip is shaped into a long, tiny needle.

Figure 3-6 shows the SEM images of the fabricated silicon microtips with the different etching mask geometries. As expected, the fabricated microtips showed different shapes according to the variation of the mask pattern. With an appropriate geometry of the SiO_2 mask, a silicon microtip with high aspect ratio and low apex

radius could be fabricated successfully.

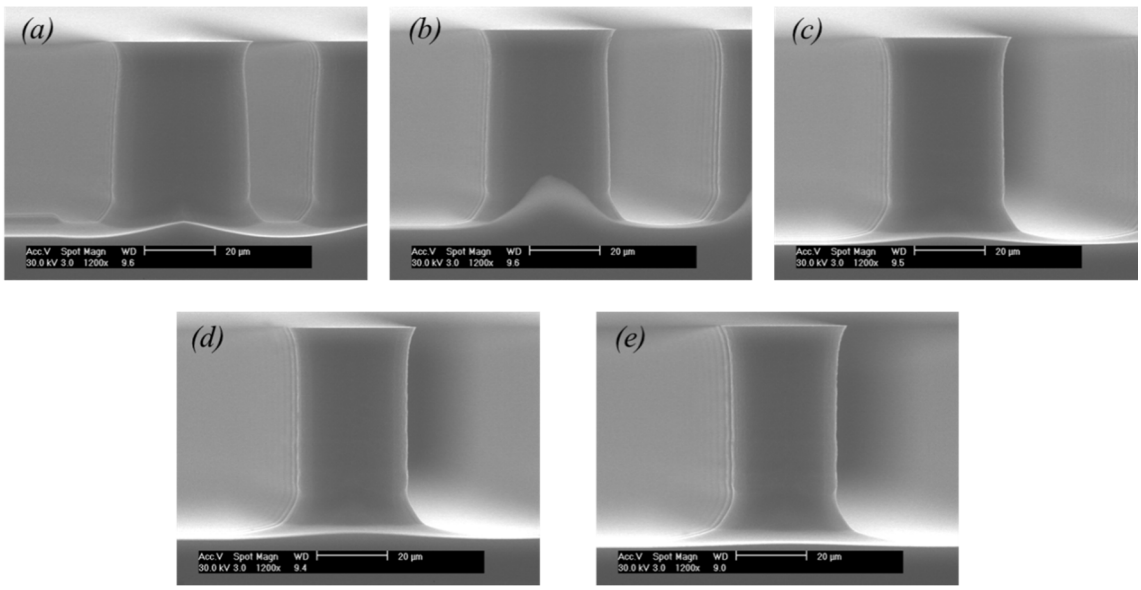

Figure 3-3. SEM images of hourglass-shaped silicon pillars after RIE etching for 3 min: (a) etching mask gap: 10 μm, (b) 20 μm , (c) 30 μm, (d) 40 μm, (e) 50 μm.

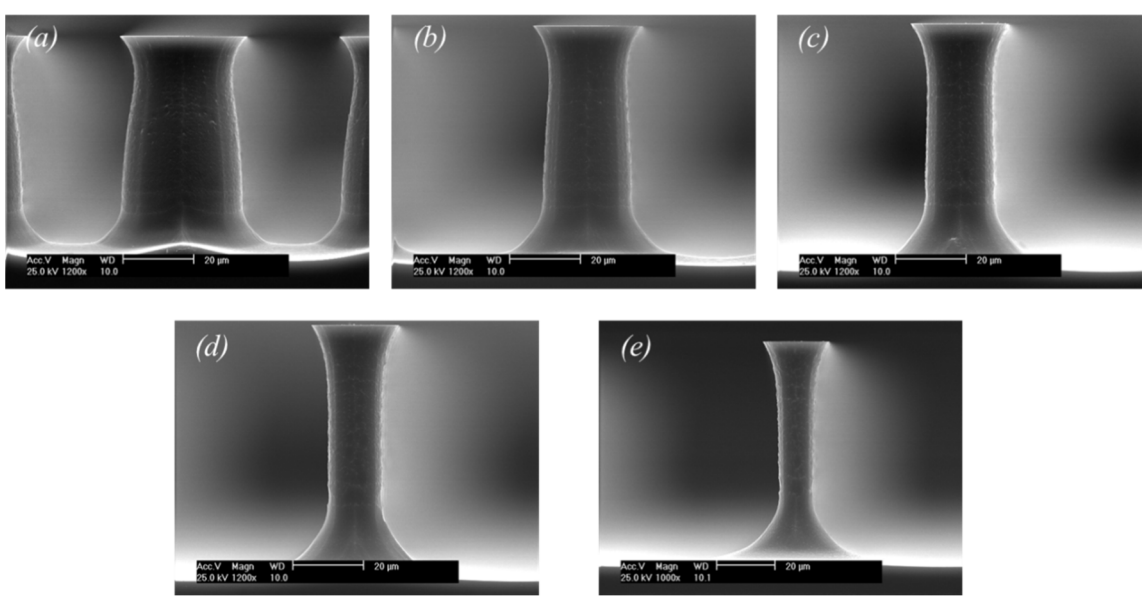

Figure 3-4. SEM images of hourglass-shaped silicon pillars after RIE etching

for 6 min: (a) etching mask gap: 10 μm, (b) 20 μm , (c) 30 μm, (d) 40 μm, (e) 50 μm.

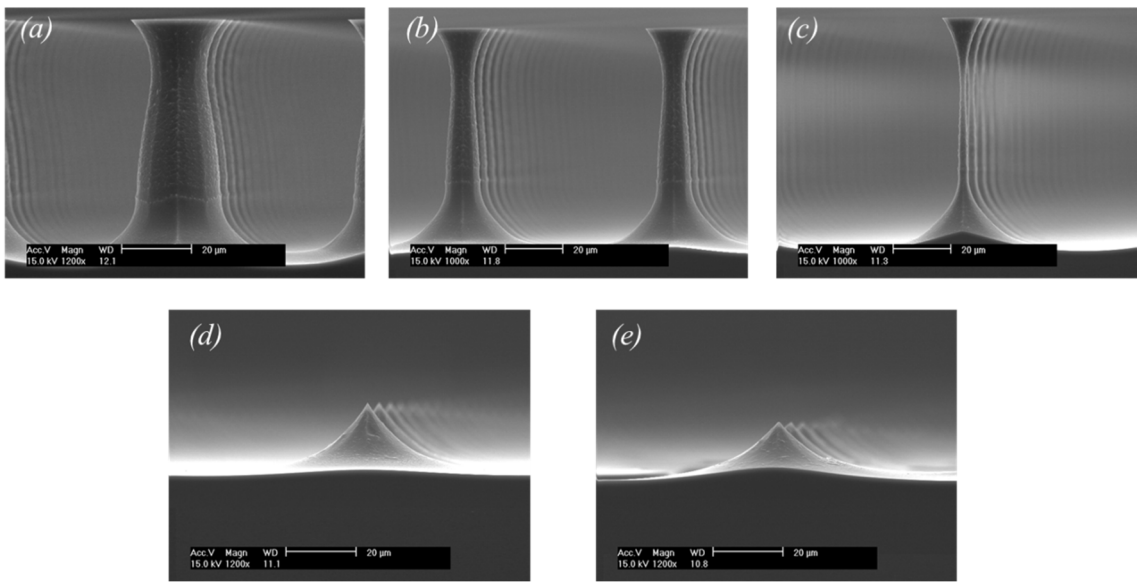

Figure 3-5. SEM images of hourglass-shaped silicon pillars after RIE etching for 9 min: (a) etching mask gap: 10 μm, (b) 20 μm , (c) 30 μm, (d) 40 μm, (e) 50 μm.

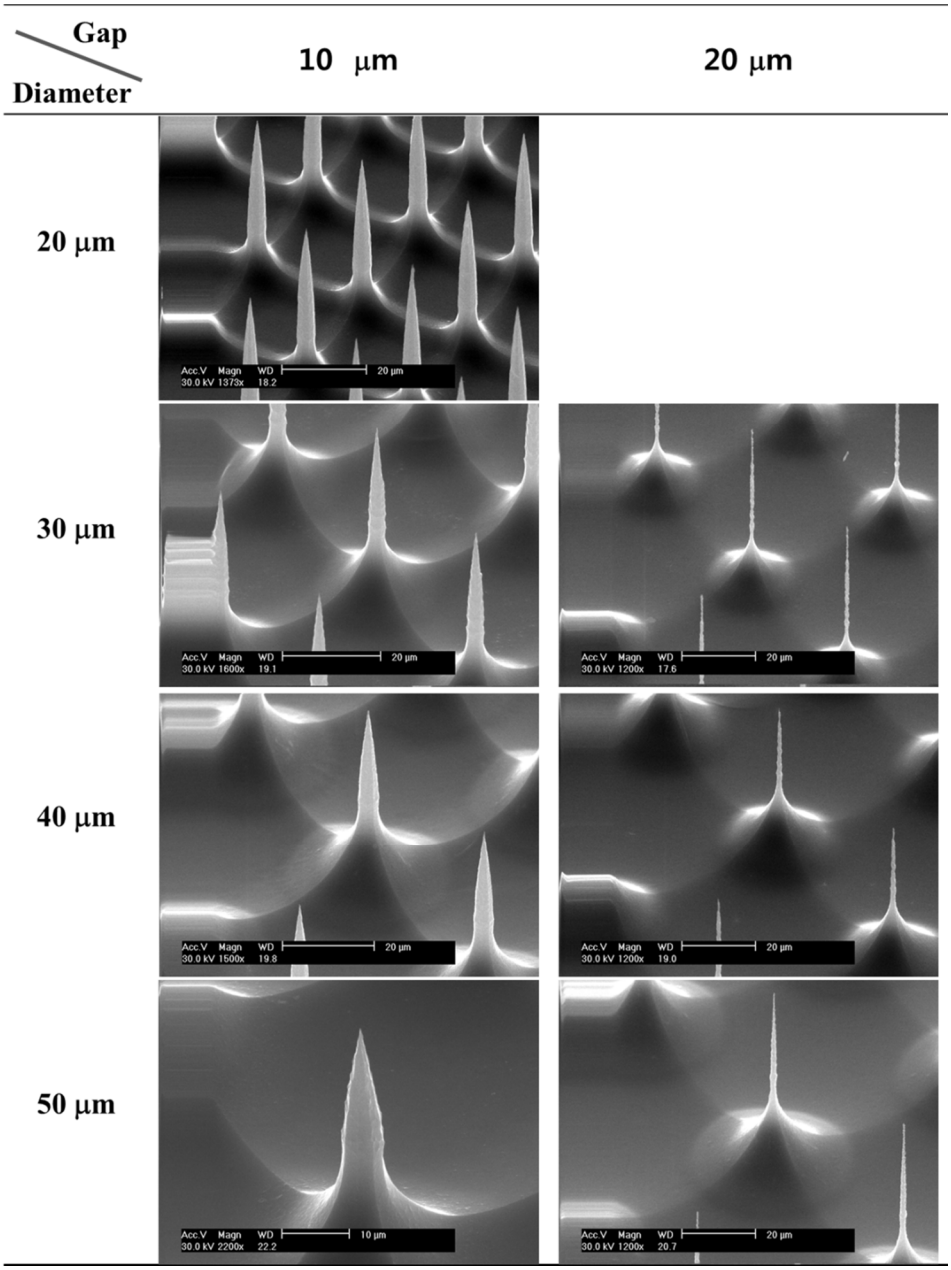

Figure 3-6. Fabricated silicon microtips.

The aspect ratio and the apex radius of the fabricated microtip were measured. We defined the aspect ratio as the height-width ratio at the top side of the microtip in the region within 5 μm from the tip end. The height (5 μm) was divided by the width measured at the point below 5 μm from the tip end to calculate the aspect

ratio. Figure 3-7 shows SEM images of the microtip obtained with a 10-μm gap and 20-μm diameter on the SiO_2 mask. The average height of the microtip is 48.7 μm. The average aspect ratio and apex radius are 6.7 and 45 nm, respectively. The measured aspect ratio and apex radius obtained with different gaps and diameters on the SiO_2 mask are shown in Figure 3-8. Generally, the aspect ratio decreases, and the apex radius increases as the etching mask diameter increases. This means that the microtip is fabricated with a more blunt conical shape when a larger etching mask diameter is used. The gap between etch masks plays a critical role in determining the shape of the microtip in this fabrication. For etching mask gaps over 20 μm, the microtips have aspect ratios less than 1 due to the high etch rate at the bottom side, which is not included in Figure 3-8.

Figure 3-9 shows the SEM images taken at each step of fabrication of the microtip electrode with a 10-μm-gap and 20-μm-diameter SiO_2 mask. The ITO film is sputtered conformally on the silicon microtip (Figure 3-9(a)), and TEOS is also deposited on the ITO film (Figure 3-9(b)). At the subsequent spin coating step, the ITO/TEOS deposited microtip is entirely covered by thick photoresist (Figure 3-9(c)). As shown in the figure, the thickness of the photoresist is reduced toward the end of the microtip, while the 20-μm-thick photoresist fills the cavity between the protruding microtips. After the RIE process with low etching selectivity between the TEOS and photoresist, the ITO film was exposed at only the tip end with submicron width. Figure 3-13 shows the fabricated microtip with a localized UME at the tip end after completion of the overall fabrication process.

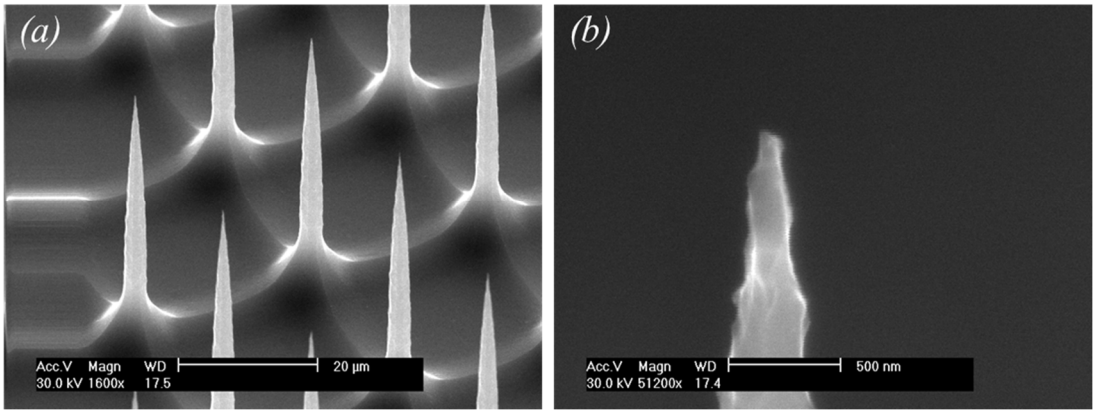

Figure 3-7. SEM images of the microtip with 10-µm gap and 20-µm diameter of the SiO_2 mask: (a) silicon microtip array, (b) close-up view of the tip end

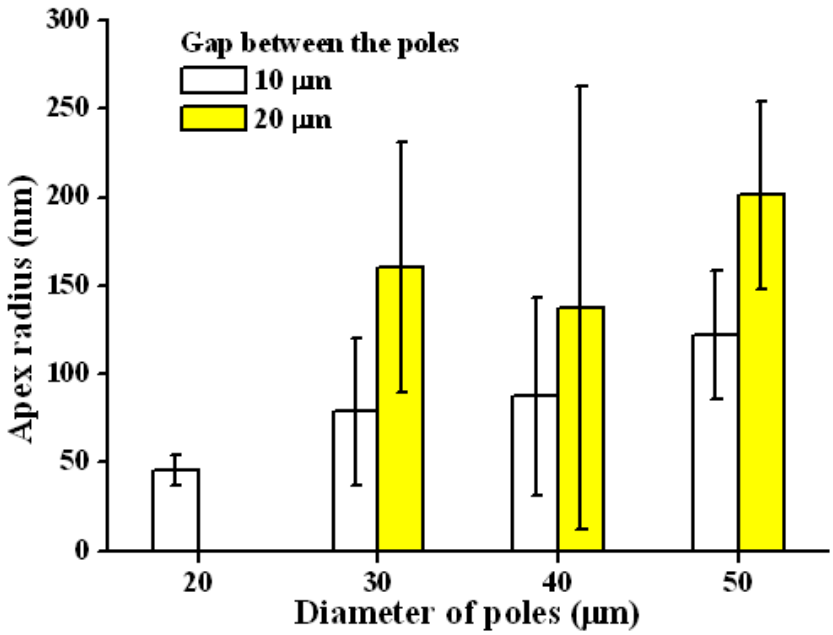

Figure 3-8. Measured results of the fabricated microtips apex radius.

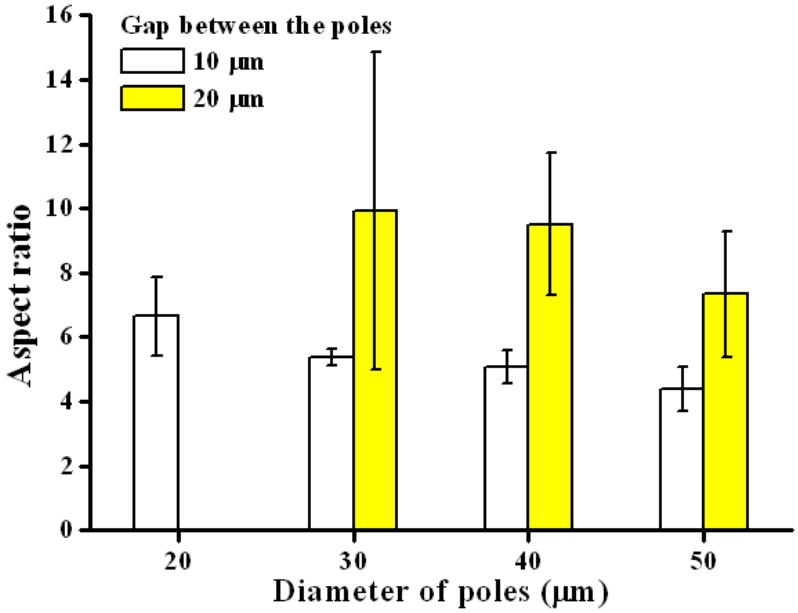

Figure 3-9. Measured results of the fabricated microtips aspect ratio.

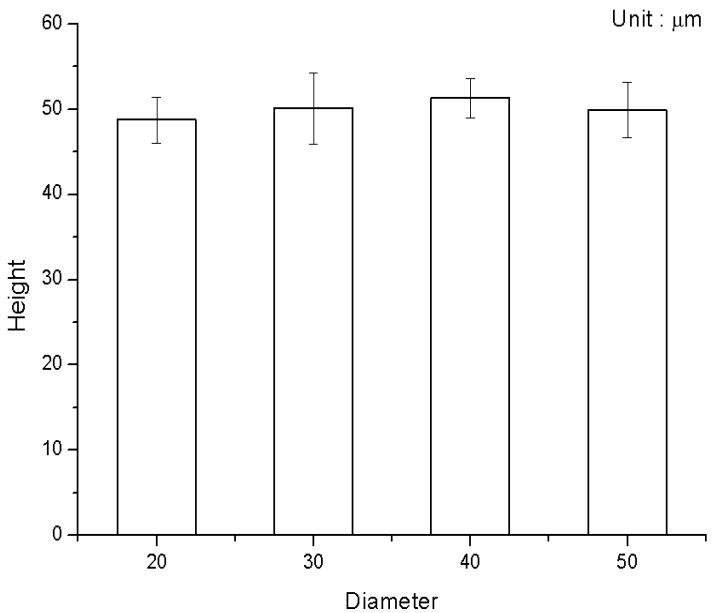

Figure 3-10. Height of fabricated microtip

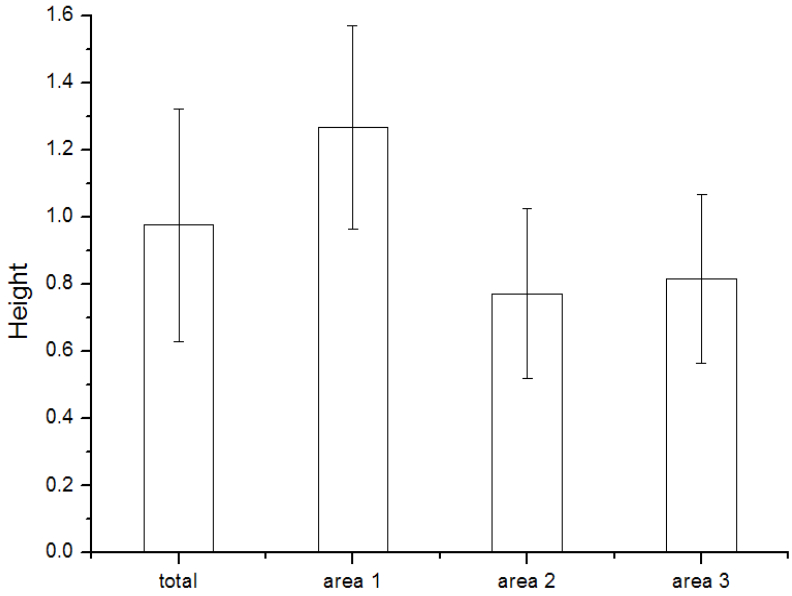

Figure 3-11. Height of fabricated exposed ITO electrode of microtip

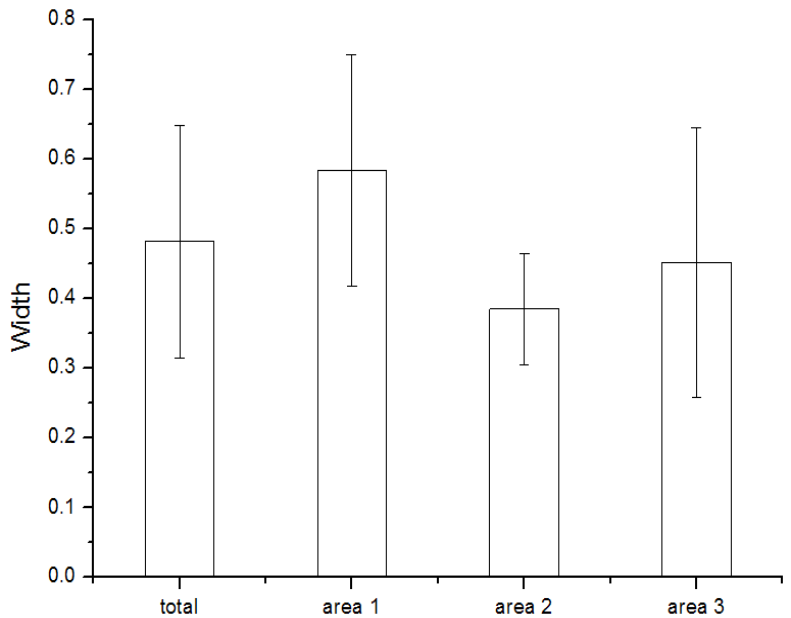

Figure 3-12. Width of fabricated exposed ITO electrode of microtip

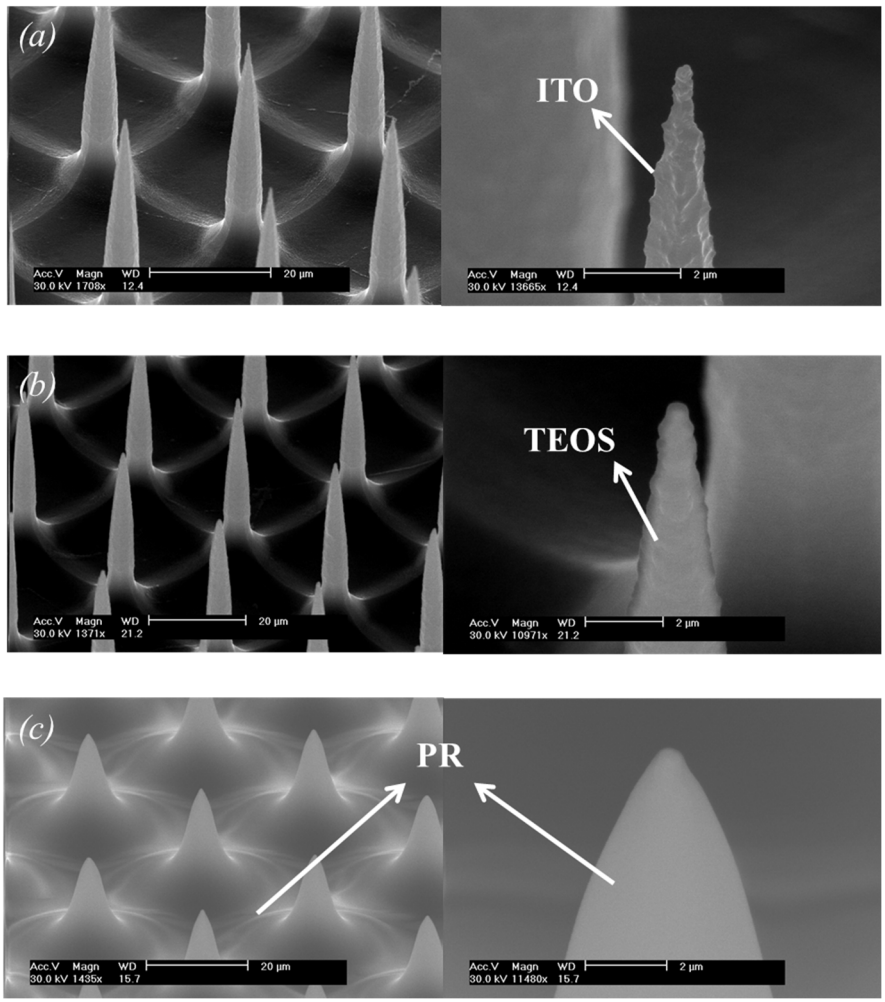

Figure 3-13. Microtip array (left) and close-up view (right) of the tip end after each fabrication process: (a) after ITO sputtering, (b) after TEOS deposition, (c) after thick PR spin coating, (etching mask gap: 10 μm, etching mask diameter: 20 μm).

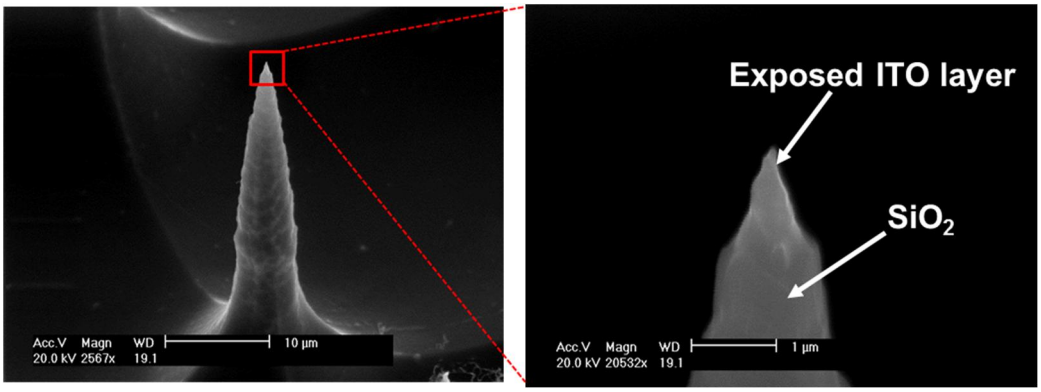

Figure 3-14. Microtip electrode with close-up view of the tip end after completion of overall fabrication process. (etching mask gap: 10 µm, etching mask diameter: 50 µm)

3.5. Electrochemical characterization

The microtip electrode array was characterized by CV. Figure 3-15 shows the experimental setup for the CV measurements. The CV measurements were performed in a three-electrode measurement setup using a potentiostat (VersaSTAT 3, Princeton Applied Research). A 100 mM $Ru(NH_3)_6Cl_3$ / 10 mM KCl solution was used as an analyte solution. The fabricated microtip electrode, an Ag/AgCl reference electrode (KCl saturated), and a Pt wire were used as working, reference, and counter electrodes, respectively.

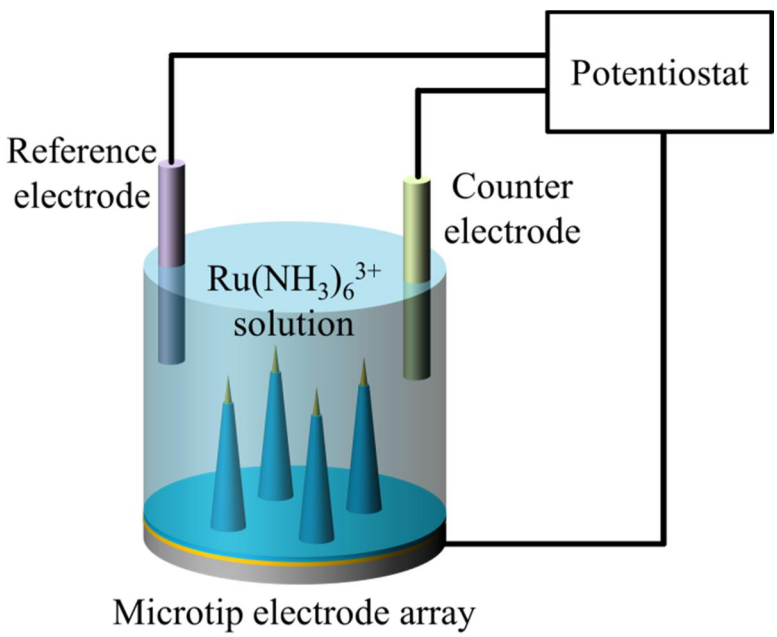

Figure 3-15. Schematic diagram of the experimental setup for CV measurements.

The CV responses of the microtip arrays with the different numbers of UMEs were measured, before and after the insulation layer removal process to expose the conducting layer at the tip ends. The CV measurement results are shown in Figure

3-16. For the microtip array without the insulation layer having been removed, the current was not measured in the CV tests. The results show that the entire conductive layer on the microtip array is completely insulated with an oxide layer. As shown in the figure, the measured current is proportional to the number of tips after removing the insulation layer at the tip end. In both cases, the UMEs of the microtip array exhibit typical behavior of a microelectrode array.

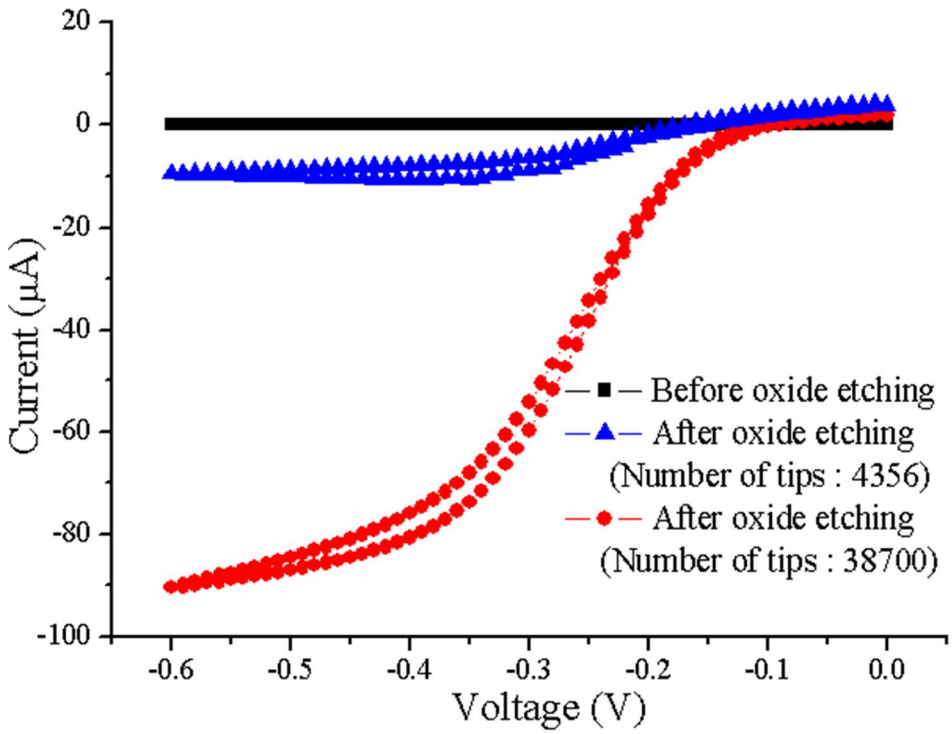

Figure 3-16. Measurement results of cyclic voltammetry.

To analyze the CV result, the limiting currents of the UME were estimated based on a conical microelectrode theory. A representative theoretical estimation of limiting current was given for a conical microelectrode by Leonhardt et al. [52]:

$$i_{conical} = \mathrm{nFDc}^{b}\mathrm{r}[A_H + B_H(R_g + C_H)^{-D_H}] \quad (3\text{-}1)$$

where n is the number of electrons transferred in the reaction, F is the Faraday constant, D is the diffusion coefficient of $Ru(NH_3)_6^{3+}$, c_b is the bulk concentration, r is the bottom surface diameter of the conical microelectrode, and R_g is the radius of the insulation sheath, which is the ratio of the insulating layer thickness and the radius of UME. The other four coefficients are determined by the aspect ratio of the UME:

$$A_H = 1.47972H + 3.69141 \quad (3\text{-}2)$$

$$B_H = 0.12629H^2 + 0.65894H - 0.01259 \quad (3\text{-}3)$$

$$C_H = 0.0115H^2 + 0.25251H - 0.72687 \quad (3\text{-}4)$$

$$D_H = -0.00943H^2 + 0.08213H + 0.83038 \quad (3\text{-}5)$$

where H is the aspect ratio, which is a ratio of the height and radius of the conical microtip. The parameters used in the estimation of the limiting current of the UME are summarized in Table 3-3. The measured peak currents for the mirotip arrays with the different numbers of UMEs were compared with the estimated values based on the conical electrode modeling mentioned above. As shown in Table 3-4, the measured peak currents were found to be in good agreement with the estimated values. This result indicates that the UMEs are localized only at the tip ends, with the rest of the areas completely insulated, and that they maintain a conical shape even after the overall fabrication process.

Table 3-3. Parameters used in the calculation of UME CV current.

Parameters	Value	Unit
Faraday constant	**9.65×10^4**	**C/mol**
Diffusivity of $Ru(NH_3)_6$	**8.8×10^{-10}**	**m^2/s**
Bulk concentration of $Ru(NH_3)_6$	**10**	**mM**
H	**4.05**	
R_g	**2.24**	

Table 3-4. Comparisons of measured current with estimated values.

Number of tips	Current (μA)		Error (%)
	Estimated value	Measured value	
38700	83.2	90.4	8.65
4356	10.2	10.6	3.92

Chapter 4. Electrochemical measurement

4.1. Materials and methods

4.1.1. Cells

Cells used in this study should be able to produce high efficiency electrical energy through photosynthesis. When energy is extracted externally through the electrode inserted into the cell, the functionality and viability of the cell should be maintained. For this purpose, Synechococcus, Chlorella, Gleobacter violaceus PCC7421 and Microcystis, which are widely used in microbial fuel cells, were cultured and supplied from a microorganism resource center (BRC). The figure below shows the images of Synechococcus cells after cell culture.

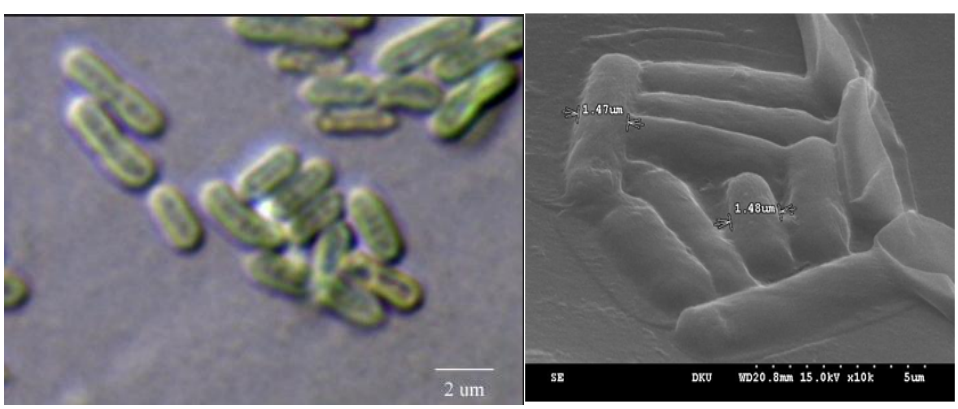

(a) (b)

Figure 4-1. Microscopic image (a) and SEM image (b) of Synechococcus [53].

As shown in the figure above, Synechococcus cells are not suitable for extraction of cell energy from chlorophyll by insertion of microtip into the cell,

with a length of 5 ~ 6 μm and a diameter of 1 ~ 2 μm. Similarly, Gleobacter violaceus, which is shown in the figure, is spherical with a diameter of 1 ~ 2 μm, so it is not suitable as a cell for microbial fuel cells because it is too small to insert microtip.

Microcystis is a primitive prokaryotic cell classified as cyanobacteria. The figure below shows the cell image of Microcystis. First, Microcystis with a size of 5 ~ 8 μm is considered to be easier to insert than other microalgae cells. Microcystis is a single cell that has no nuclear membrane like bacteria. It is a photosynthetic cell with chloroplast and has low resistance to electrodes, high efficiency of cell energy extraction.

Haematococcus which is a large sized green algae cell was also selected and cultured in order to study the insertion of electrodes into microalgae cells more efficiently. Haematococcus is a spherical photosynthetic cell with a diameter of 50 ~ 60 μm. It is very advantageous for insertion of the electrode. It contains the chlorophyll a, chlorophyll b, carotene, xanthophyll, etc. However, it has a drawback that membrane of the cell is too hard to insert micotip in the cell. The Figure 4-2 below shows the Haematococcus and Microcystis cell image.

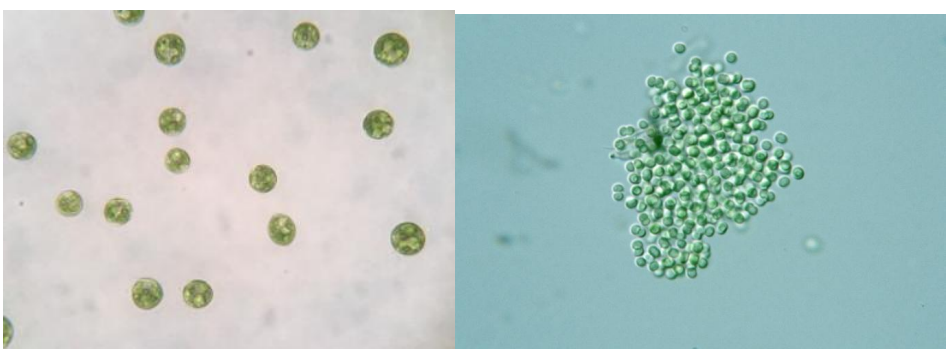

(a) (b)

Figure 4-2. Microscopic image of (a) Haematococcus [54] and (b) Microcystis [55].

Chlorella is a spherical cell with a diameter of 2 ~ 10 μm and is useful for electrode insertion. There are cell walls and nuclear membranes, but they have relatively thin cell walls compared to other cells. It contains chlorophyll a and b pigment and has high photosynthetic ability due to high concentration of chloroplast, which is advantageous for energy extraction.

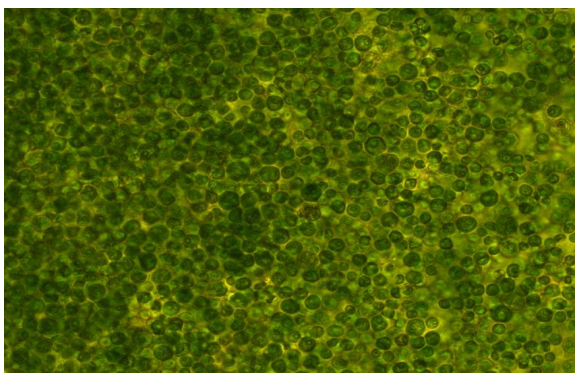

Figure 4-3. Microscopic image of Chlorella

In this paper, there are three major requirements for cell selection. First, size and shape should be appropriate to ensure ease of experiment. Secondly, it has low resistance to microtip due to the absence of nuclear membrane and low mechanical strength of cell wall. Finally, since chlorophyll is distributed evenly in the cells, high cell energy efficiency should be obtained when the microtip is intracellularly inserted. Considering the above requirements, Chlorella was selected as a microalgae cell for microbial fuel cells.

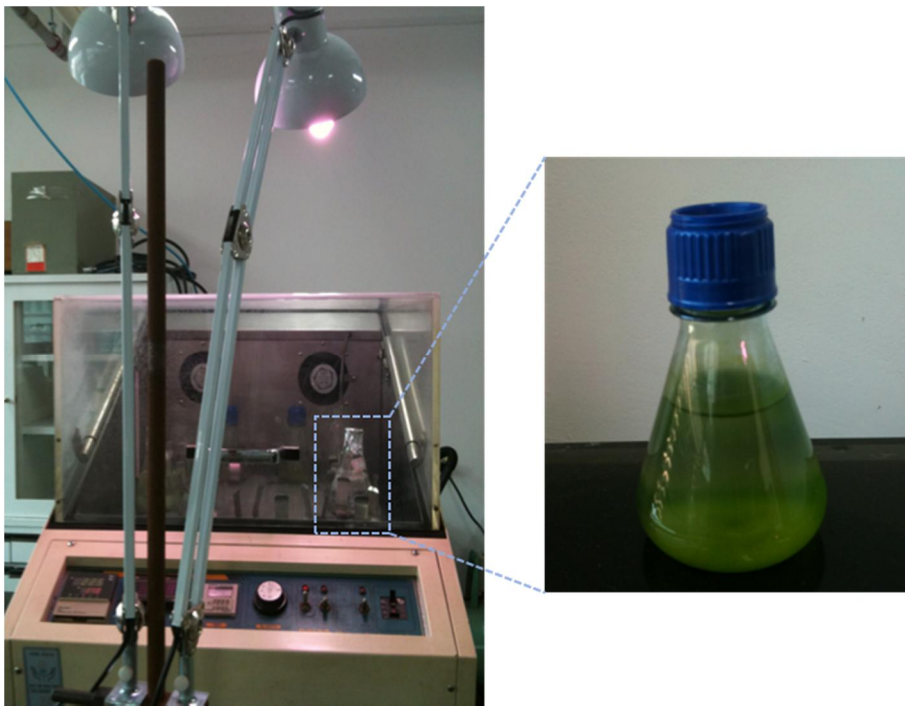

Figure 4-4. The cell culture system and the cell culture medium in which the concentrated cells are suspended

In order to efficiently and stably extract the electrical energy generated by photosynthesis, it is essential to develop a culture technique that ensures the cell's functionality and viability. In this study, we developed an optimized culture system considering the growth environment of selected cells.

The cell culture temperature was 26 ° C and the density of light required for photosynthesis was maintained at 2000 to 3000 lux. Considering the characteristics of selected cyanobacteria, BG11 cell culture medium containing a small amount of organic matter was prepared. On the other hand, it is necessary to actively control the cell concentration in order to insert the electrode into the cell by using the microfluidic device and the microtip electrode. Therefore, a centrifuge was used in this study. The Figure 4-4 shows a cell culture in which cells concentrated by centrifugation are suspended.

(a)

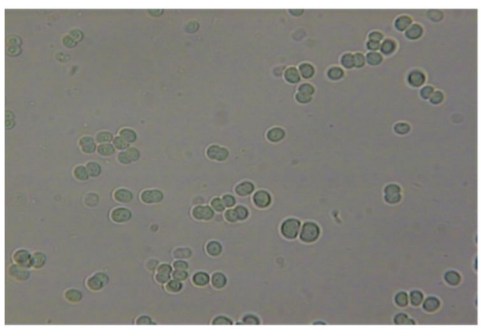

(b)

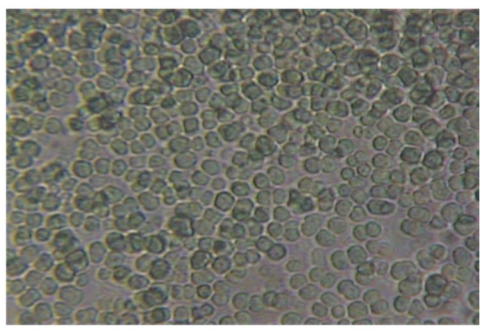

(c)

Figure 4-5. (a) Cell concentration control using a centrifuge (b) Before concentration control (c) After concentration control

4.1.2. Insertion of the microtip array into the cells in the microfluidic chamber

First, the microtip array was fixed on a fiber optic alignment stage (Newport Corp. USA). Then the microfluidic chip was placed on top of the microtip array. The insertion of the microtip array into the microfluidic chamber through the thin PDMS layer was conducted using the fiber optic alignment stage, while fixing the microfluidic chamber. The fiber optic alignment stage allowed precise control of

the insertion of the microtip array. Figure 4-6 shows the PMFC after inserting the microtip array into the microfluidic chamber.

In order to confirm the penetration, the current between an anode on the microtip array and a cathode on the microfluidic chamber was monitored in the course of insertion. Once the microtip array penetrated into the microfluidic chamber, the current between UMEs of the microtip and a microelectrode in the microfluidic chamber began to flow. In addition, Figure 4-7 shows that SEM image was taken after penetration into the microfluidic chamber.

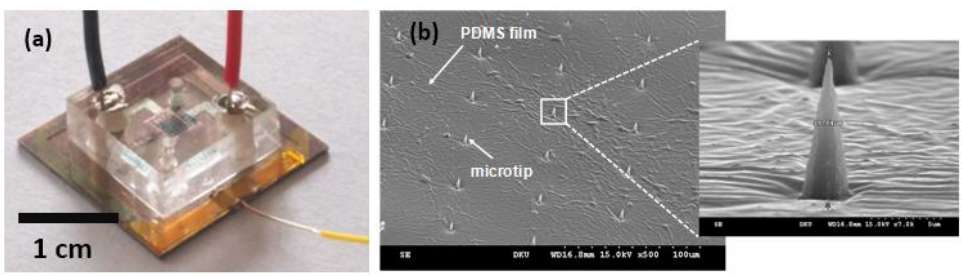

Figure 4-6. Assembled microtip and microfluidic chip.

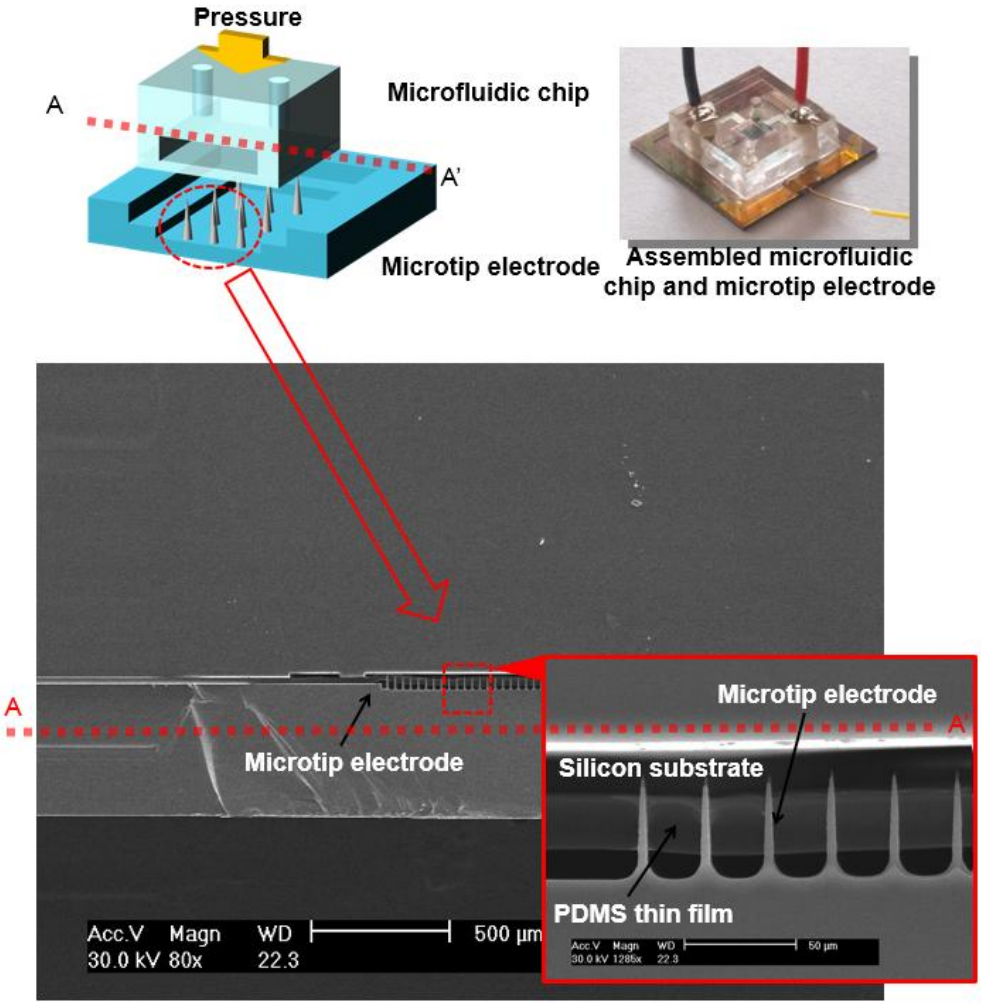

Figure 4-7. SEM image taken after penetration into the microfluidic chamber.

4.2. Measurement results

4.2.1. Short circuit current measurement

Figure 4-8 shows that short circuit current was recorded as a function of time before and after the microtip array penetrated cells. Before the UMEs on the microtip array were inserted through the PDMS layer, no current flowed between the UMEs and the microelectrodes in the microfluidic chamber. However, when the microtip array was slightly inserted into the chamber through the thin PDMS layer, short circuit current began to flow. The current did not respond to light stimulation, which indicates that the UMEs on the microtip array did not penetrate the cells. When the microtip array was inserted further into the microfluidic chamber, the short circuit current responded to the light stimuli. The current increased as a result of the light illumination, and decreased when the light was removed. When the microtip array was inserted further, the response was the same, which meant that the UMEs of the microtip array were still placed inside the cells.

The light induced current may originate from the high-energy electrons generated during photosynthesis. It has been demonstrated that several metal electrodes can be used for harvesting electrons from photosynthesis-related molecules [56, 57]. Therefore, in this research, the invasive UMEs may have withdrawn electrons generated during photosynthesis. After that, the high-energy electrons were transferred to the microelectrode in the microfluidic chamber, and reduced with dissolved oxygen and protons.

The photocurrent was about 200 times larger than that recorded with a single UME used for single cell measurement [28]. However, this current for the microtip array with 17689 UMEs was not high. This low current may have resulted for two

reasons. First, a large portion of the UMEs on the microtip array did not penetrate cells, and stayed in the cell medium. Therefore, only a small portion of UMEs of the microtip array was used to draw electrons from the cells. Second, a considerable amount of the high-energy electrons generated during the photosynthesis was reduced with oxygen molecules and protons on the UMEs of the microtip array, instead of being reduced on the cathode in the microfluidic chamber. That is, an internal closed circuit on the UMEs of the microtip array prevented the high-energy electrons from reaching the cathode in the microfluidic chamber.

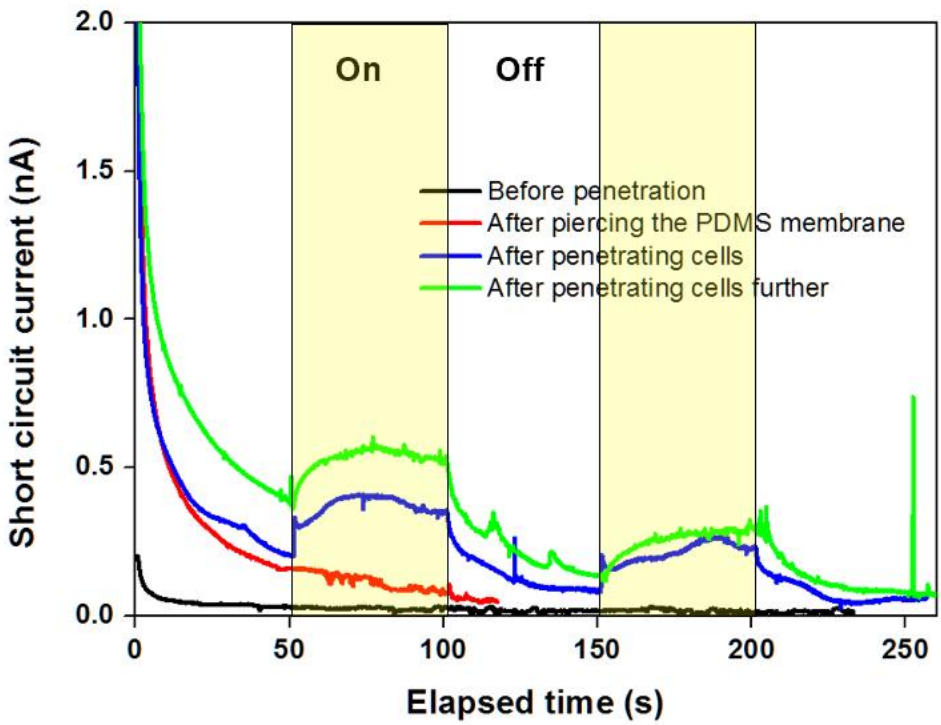

Figure 4-8. Short circuit current measurement over time before, and after penetrating a PDMS membrane and cells in the microfluidic chamber

4.2.2. Open circuit voltage measurement

The open circuit voltage (OCV) was measured, and yielded a similar result, as shown in Figure 4-9. When the microtip array was outside the microfluidic chamber, the OCV was zero. When the microtip array was slightly inserted into the microfluidic chamber, the OCV was measured, but did not respond to light stimuli. However, as the microtip array was inserted into the cells, the OCV responded to the light input, and increased, depending upon the light input.

As the redox potentials of photosynthesis related proteins range from 380 mV to -420 mV with respect to a normal hydrogen electrode, the ideal OCV of PMFC calculated by the Nernst equation ranges from several hundred mV to over 1000 mV. However, the measured OCV was less than 50 mV, even under a light irradiation condition. This indicates that both photosynthesis related oxidation and oxygen reduction occurred simultaneously, and formed a mixed potential on the UMEs of the microtip array. Consequently, the OCV was lower than anticipated.

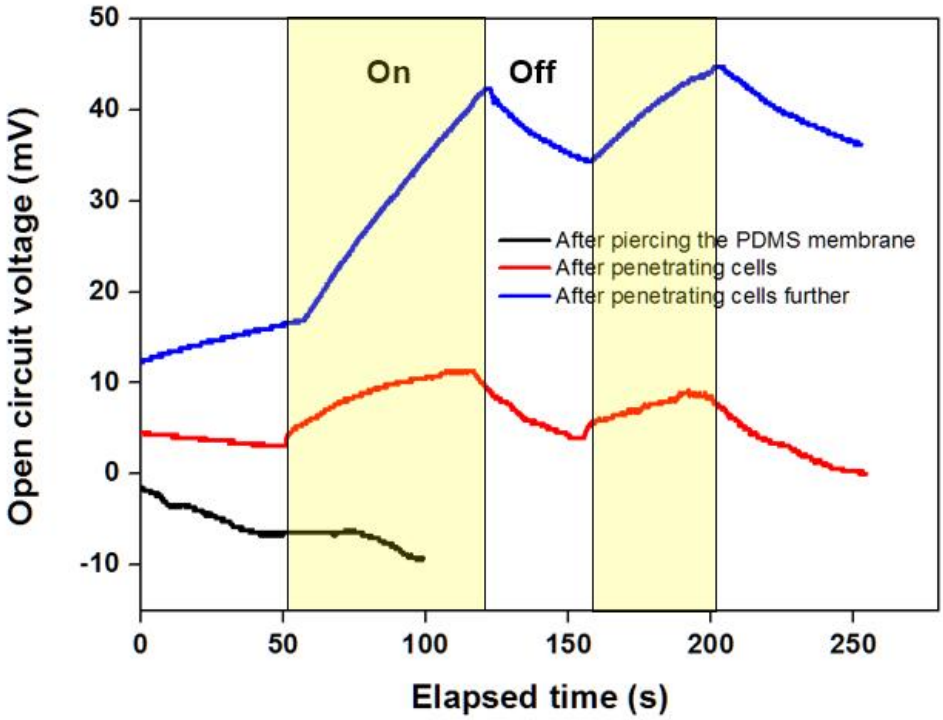

Figure 4-9. OCV measurement over time before, and after penetrating a PDMS membrane and cells in the microfluidic chamber.

4.2.3. Prediction of relation between light quantity and current

The light source used in this paper is a titanium halogen lamp. The light intensity measured in the same environment as the experiment is 20800 lx. The photosynthetic photon flux density (PPFD) of the wavelength band corresponding to the visible light ray region (400 nm ~ 700 nm), known as the photosynthetically active radiation region, is used for the photosynthesis experiment. The conversion of the amount of titanium halogen lamp used in this experiment to PPFD is 416 μmoles / m^2 / s [58]. This value is 3.85 times larger than 108 μmoles / m^2 / s, which is the maximum amount of current measured by Stanford University [28].

Based on the data reported by Stanford University, it can be seen that the

magnitude of the current increases with the increase of the amount of light in the Figure 4-10(a). Figure 4-10(b) shows the concentration of oxygen produced by photosynthetic cells according to the amount of light.

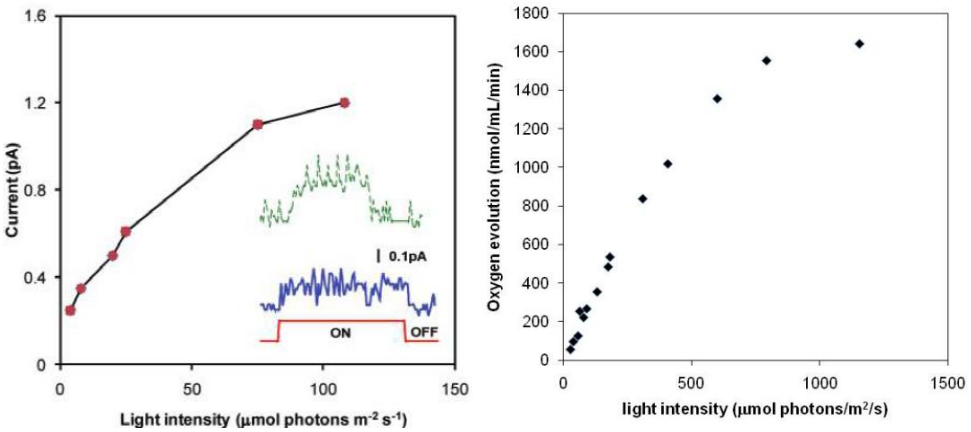

(a) (b)

Figure 4-10. Light intensity data reported by Stanford University [28] (a) Change of current according to light quantity (b) Change of oxygen concentration according to light amount

The change of the standard electrode potential according to the concentration of the reactant increases together with the increase of the oxygen concentration according to the following Nernst equation. If the concentration of oxygen around the counter electrode increases as shown in the Figure 4-10(b) due to photosynthesis, the electrode potential of the counter electrode reaction that oxygen molecules and hydrogen ions are changed into water is increased. As a result, it is expected that the magnitude of the current flowing through the electrode will increase.

$$E^{0\prime} = E^{0} - \frac{RT}{nF}\ln\left(\frac{[H_2O]}{[O_2]^{1/2}[H^+]^{1/2}}\right) \qquad (4\text{-}1)$$

Chapter 5. Loss analysis and discussion

5.1. Introduction

The loss analysis of the measured current values as described in the previous chapter was conducted in two ways. First, the reduction of the measured current due to the distance between the working electrode and the counter electrode was verified by electrochemical simulation. As the distance between the working electrode and the counter electrode increases, the magnitude of the current due to the resistance of the electrolyte decreases.

The factors affecting the simulation of the electrochemical reaction are cell geometry, cell operating condition, electrolyte conductivity, electrode kinetics, and mass transport of ions in the electrolyte. The simulation of this paper was carried out by varying the distance between the working electrode and the counter electrode, with the cell geometry as the main parameter and the other conditions being the same as the experimental conditions.

The second factor of the current reduction is the deformation of the PDMS chamber by a microtip electrode moving vertically during assembly. In order to analyze the effect of the deformation on the reduction of the measuring current, the deformation due to the low stiffness of the thin PDMS film was measured and the effective area in the assembly process was calculated by deformation.

5.2. The electrochemical simulation of current reduction by distance between electrodes

5.2.1. Governing equations for simulation

When modeling an electrochemical cell, it is necessary to calculate the voltage and current density at the surface reaction between electrode and electrolyte, and at the electrode and electrolyte, respectively. Since a metal conductor is generally used as an electrode in an electrochemical cell, the current flow in the electrode follows the Ohm's law.

$$j_s = -\sigma_s \nabla \phi_s \ , \ \frac{\partial \rho}{\partial t} + \nabla \cdot j_s = 0 \tag{5-1}$$

where, j_s denotes the current density vector (A/m^2) in the electrode, σ_s denotes the conductivity (S/m), ϕ_s denotes the electric potential in the metallic conductor (V), and ρ denotes an electric charge density (C/m^3). In the electrolyte, which is an ionic conductor, the net current density can be described using the sum of fluxes of all ions.

$$j_l = F \sum_i z_i N_i \tag{5-2}$$

where j_l denotes the current density vector (A/m2) in the electrolyte, F denotes the Faraday constant (C/mol), and N_i the flux of species (mol/(m^2·s)) with charge number z_i. The flux of an ion in an ideal electrolyte solution is described by the Nernst-Planck equation and accounts for the flux of solute species by diffusion, migration in the two respective additive terms.

$$N_i = -D_i \nabla c_i - z_i u_{m,i} F c_i \nabla \phi_l \tag{5-3}$$

where c_i represents the concentration of the ion i (mol/m^3), D_i the

diffusion coefficient (m^2/s), $u_{m,i}$ its mobility (s·mol/kg), ϕ_l the electrolyte potential. On substituting the Nernst-Planck equation into the expression for current density, we find following equation.

$$j_l = -F(\nabla \sum_i z_i D_i c_i) - F^2 \nabla \phi_l \sum_i z_i^2 u_{m,i} c_i \quad (5\text{-}4)$$

with conservation of current including a general electrolyte electric charge density term ρ (C/m^3).

$$\frac{\partial \rho}{\partial t} + \nabla \cdot j_s = 0 \quad (5\text{-}5)$$

If the charge transfer process determines the overall reaction rate in the electrochemical reaction $O + ne = R$, the reaction rate of the forward reaction (v_f), reverse reaction (v_b) and i_{net} are expressed as follows.

$$v_f = k_f C_O(0,t) = \frac{i_c}{nFA}\ ,\ v_b = k_b C_R(0,t) = \frac{i_a}{nFA}\ ,\ v_{net} = v_f - v_b = \frac{i_{net}}{nFA}$$

$$i_{net} = i_c - i_a = nFA[k_f C_O(0,t) - k_b C_R(0,t)] \quad (5\text{-}6)$$

Here, $C_O(0,t)$ and $C_R(0,t)$ represent the concentrations of O and R at the electrode surface because only O or R present near the electrode surface can participate in the charge transfer process. In electrochemical reactions, the rate constants of the forward and reverse reactions are expressed in the following equations.

$$k_f = k^0 e^{-\alpha nF(E-E^{0'})/RT}\ ,\ k_b = k^0 e^{(1-\alpha)nF(E-E^{0'})/RT} \quad (5\text{-}7)$$

Where k^0 is the standard rate constant, α is the symmetry factor, and E is the voltage applied to the electrode. From this equation, it can be seen that the reaction rate constant varies exponentially with the voltage applied to the electrode. i_{net} can be rearranged as follows using the above equation. The first term on the right side refers to the reduction current and the second term refers to the oxidation current.

$$i_{net} = i_c - i_a = nFAk^0\left[C_O(0,t)e^{-\alpha nF(E-E^{o'})/RT} - C_R(0,t)e^{(1-\alpha)nF(E-E^{o'})/RT}\right] \quad (5\text{-}8)$$

In equilibrium, $i_{net} = 0$, but the same current actually flows in both directions, which is called the exchange current (i_0). In the equilibrium state, $i_0 = i_c = |i_a|$, the exchange current can be derived as follows. At the equilibrium state ($E = E_{eq}$), exchange current is derived as follows.

$$i_0 = i_c = nFAk^0 C_O^* e^{-\alpha nF(E_{eq}-E^{0'})/RT} \quad (5\text{-}9)$$

In the equilibrium state, the surface concentration and the bulk concentration are the same, so the concentration is described as the following equation.

$$C_O(0,t) = C_O^* \ , \ C_R(0,t) = C_R^* \quad (5\text{-}10)$$

The equation of i_0 is derived from the equilibrium voltage below.

$$E_{eq} = E^{0\prime} + \frac{RT}{nF}\ln\frac{C_O^*}{C_R^*} \quad (5\text{-}11)$$

$$\frac{C_O^*}{C_R^*} = e^{nF(E_{eq}-E^{0'})/RT} \ , \ \left(\frac{C_O^*}{C_R^*}\right)^{-\alpha} = e^{-\alpha nF(E_{eq}-E^{0'})/RT} \quad (5\text{-}12)$$

$$i_0 = nFAk^0 C_O^{*(1-\alpha)} C_R^{*\alpha} \quad (5\text{-}13)$$

From the above equation, the current flow on the electrode surface can be summarized as follows.

$$i_{net} = i_0\left[\frac{C_O(0,t)}{C_O^*}e^{-\alpha nF(E-E_{eq})/RT} - \frac{C_R(0,t)}{C_R^*}e^{(1-\alpha)nF(E-E_{eq})/RT}\right] \quad (5\text{-}14)$$

In the above equation, the preceding term refers to the reduction current of O and the latter term refers to the oxidation current of R. The term expressed as the ratio of the concentration means the mass transfer rate, and the term given as an exponential function of the overvoltage means the charge transfer rate.

In equation (5-14), $\frac{C_O(0,t)}{C_O^*} = \frac{C_R(0,t)}{C_R^*} = 1$ is established when the mass transfer rate in the electrochemical reaction is sufficiently large so that the entire rate determining step is a charge transfer process. Therefore, equation (5-14) is rearranged into equation (5-15).

$$i_{net} = i_0\left[e^{-\alpha nF\eta/RT} - e^{(1-\alpha)nF\eta/RT}\right] \quad (5\text{-}15)$$

This is called the Butler-Volmer equation, which shows how the current varies with the applied voltage when the charge transfer process determines the rate. Since $\eta = E\text{-}E_{eq}$, when the electrode potential is changed to a negative value, the former term (reduction current) increases by the exponential function, and the latter term (oxidation current) decreases by the exponential function. Conversely, when the electrode potential is changed to a positive value, the reduction current is decreased by the exponential function because η has a positive value. Instead, the oxidation current increases by the exponential function.

5.2.2. Simulation conditions

The basic chemical reaction is as follows. The electrons generated as the ferredoxin is oxidized in the anode move to the cathode through the electrode. In Cathode, oxygen and hydrogen ions combine with electrons transferred to form H_2O and form a current loop.

$$\text{Anode :} \quad Fd^{2+} \rightarrow Fd^{3+} + e^-$$

$$\text{Cathode :} \quad O_2 + 4H^+ + 4e^- \rightarrow 2H_2O$$

The simulation parameters such as equilibrium voltage and reaction constants are summarized in Table 5-1.

Table 5-1. Values used for variables and constants used to calculate the theoretical value

Parameter	Value	Note	Reference
$\mathbf{V_{eq\_a}}$	-0.43 V	Anode reference potential	
$\mathbf{V_{eq\_c}}$	0.76 V	Cathode reference potential	
$\mathbf{H^+}$	1×10^{-7} M	Concentration	
Ferredoxin	2.5×10^{-3} M	Concentration	[59]
$\mathbf{O_2}$	2.48×10^{-4} M	Concentration	
σ	0.2145 S/m	Electrolyte conductivity	
D	1×10^{-9} m^2/s	Diffusion constant of H^+	
$\boldsymbol{i_0}$ **at anode**	2.4 A/m^2	Exchange current of anode reaction	
$\boldsymbol{i_0}$ **at cathode**	2.2×10^{-7} A/m^2	Exchange current of cathode reaction	
Chlorella conductivity	8 mS/m	Cell conductivity	[60]
	0.02 mS/m	Membrane conductivity	

In this study, electrochemical analysis of one cell was performed using COMSOL Multiphysics (ver. 4.4), a commercial FEM simulation program. The Secondary Current Distribution interface in COMSOL program is used for setting up the model for the currents in the electrolyte and electrodes. Secondary current distribution assumes that electricity moves through the electrolyte only as ionic migration, while the reactions at the electrodes are a function of the electric potential and local concentration of reacting species. Transport of Diluted Species

interface is also used to simulate the movement of hydrogen ions. Ohm's law is therefore applied, together with a charge balance, to solve for the electric currents in the electrodes and the electrolyte, which are also coupled to concentration dependent kinetics and Butler-Volmer expressions that describe the electrochemical reactions.

5.2.3. Simulation geometries

The three - dimensional domain constructed for electrochemical analysis was analyzed in two ways. First, the model of the study in which the electrons were extracted from photosynthesis in a single algae cell was simulated and compared with the simulation of this study model. At Stanford University, Ryu et. al. have extracted electrons from the photosynthetic algal cells using sharp electrode [28]. In this study, nanoprobes were inserted into cells using an AFM controller. This study measured the magnitude of current up to 1.2 pA on a single cell based extraction.

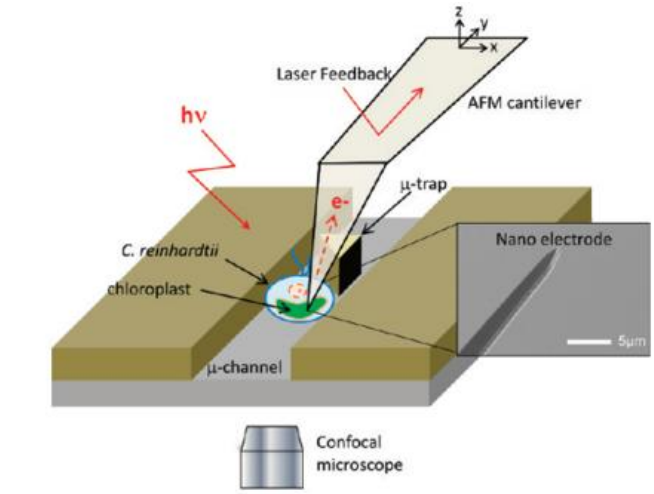

(a)

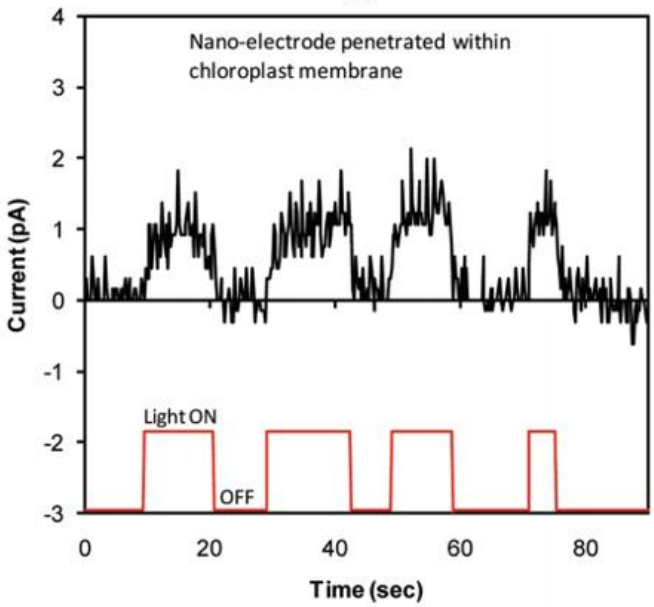

(b)

Figure 5-1. Stanford model (a) Single cell platform with nanoprobe and AFM controller (b) Measured current extracted from single cell [28].

The geometry of the Stanford model simulation in this study is as follows. The cathode is located at the bottom of the anode, with a width of 240 μm and a length of 1 mm. In the center of the cathode, a fluidic channel with a width of 20 μm and a depth of 10 μm is located. Anode was inserted in the center of cells with a size of 9 μm and was designed as a rectangular parallelepiped with a length of 10 μm and a

width of 1 μm. The electrochemical reaction was set up to occur only on the 1 μm × 1 μm wide surface of the electrode.

The cell size was set to 9 μm in diameter and the cell membrane thickness to 0.1 μm. To simulate the measurement with short circuit current, the value of the current flowing in the bar with low resistance was calculated by connecting the metal bar between anode and cathode.

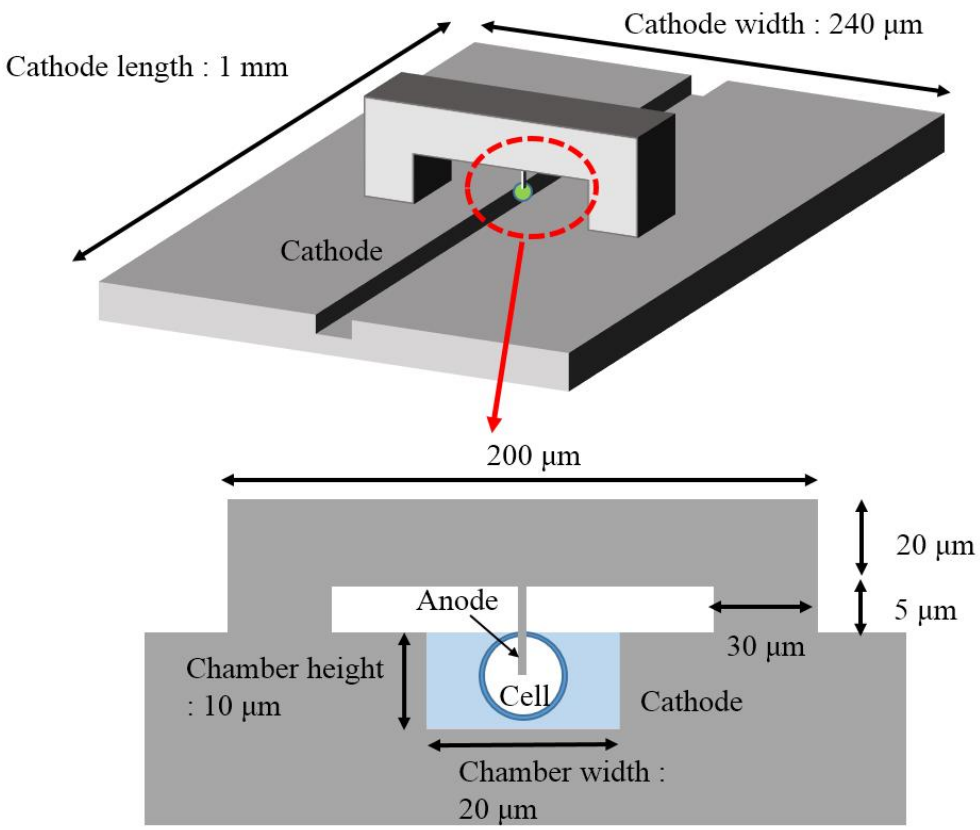

Figure 5-2. Schematic diagram of the simulation geometry of Stanford model

The geometry of the model in this study is as follows. The size of the chamber was designed as 3.5 mm × 3.5 mm × 10 μm. The inside of the chamber is filled with electrolyte. The cathode is located at one end of the chamber and is designed as 3.4 mm × 800 μm × 1.5 μm. Anode was inserted in the center of cells with a size

of 9 μm and was designed as a rectangular parallelepiped with a length of 10 μm and a width of 1 μm. The electrochemical reaction was set up to occur only on the 1 μm × 1 μm wide surface of the electrode. The distance between the anode and the cathode is 150 μm ~ 2150 μm.

The cell size was set at 9 μm in diameter and the thickness of the cell membrane was 0.1 μm. To simulate the measurement with short circuit current, the value of the current flowing in the bar with low resistance was calculated by connecting the metal bar between anode and cathode.

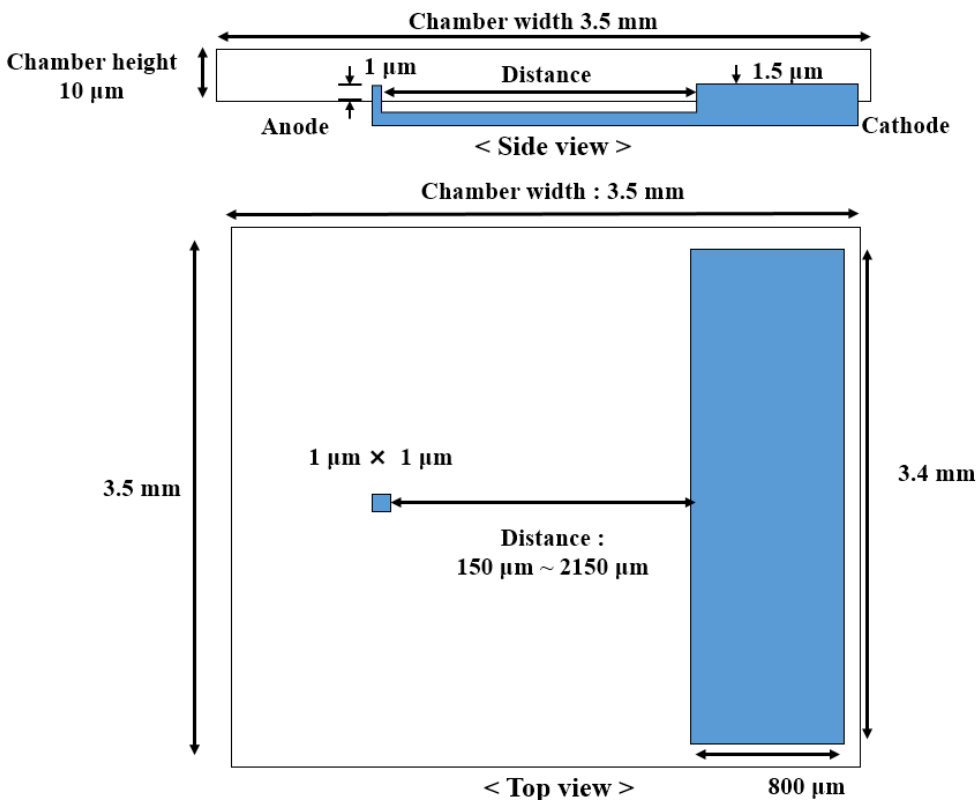

Figure 5-3. Schematic diagram of simulated geometry of this work

5.2.4. Simulation results

The magnitude of current extracted from single cells in each model is shown in the following table. When the anode is located inside the cell, the current is smaller than without cell. This is predicted due to the low conductivity of cell membrane and inside of the cell. In the case of the Stanford model and our model, the distance between the anode and the cathode was designed to be 5 μm and 150 μm, respectively.

Table 5-2. Simulation results of Stanford model and this work.

Simulation model	*Simulated value*	*Note*
Stanford Univ.	52.3 pA (1 cell)	w/o cell
	29.8 pA (1 cell)	w/ cell
This work	40.1 pA (1 cell)	w/o cell
(distance between electrodes : 150 μm)	24.7 pA (1 cell)	w/ cell

In this study, the magnitude of the current varies with the distance between the electrodes. The distance between electrodes was simulated for a total of 11 intervals from 150 μm to 2150 μm. The leftmost point is simulated in this study model when the distance between electrodes is 5 μm as in the Stanford model. The currents were simulated at 35.7 pA when the distance between electrodes was 5 μm and 24.7 pA and 16.0 pA at 150 μm and 2150 μm, respectively. It can be seen that 69% and 45% of the current flows compared to when the distance between the electrodes is 5, respectively.

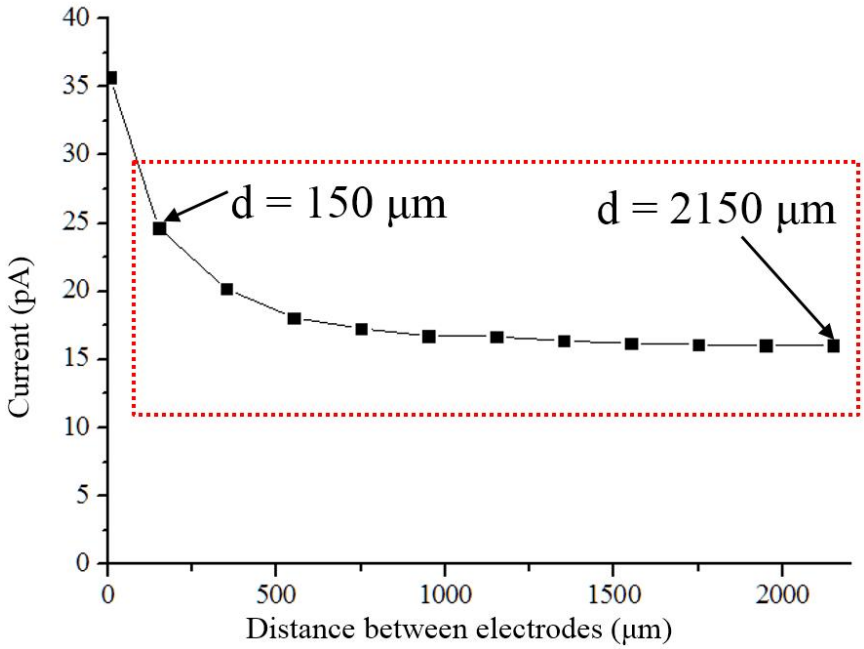

Figure 5-4. Simulated current with different distance between electrodes

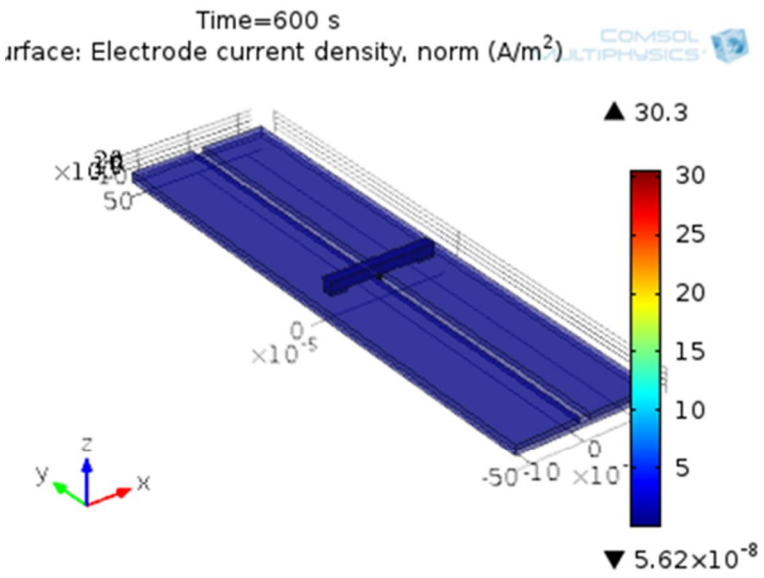

(a)

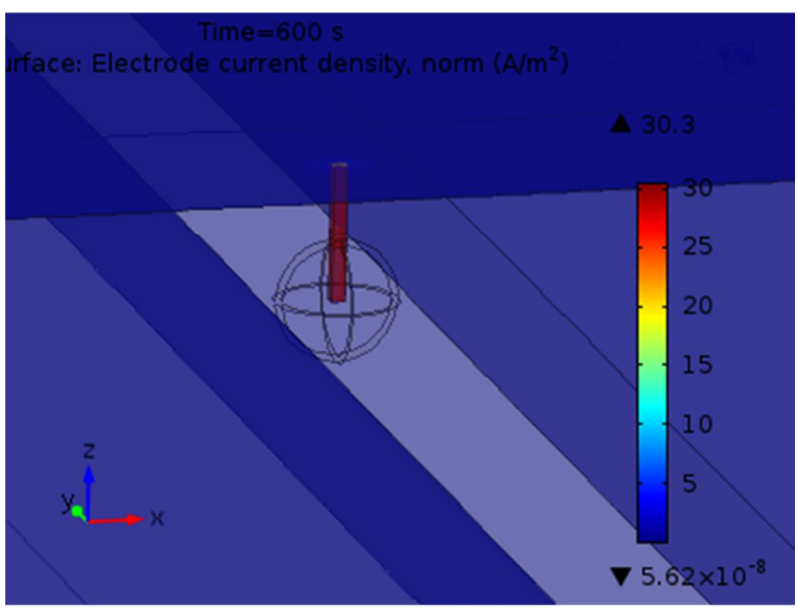

(b)

Figure 5-5. Simulated electrode current density of Stanford model (a) whole geometry (a) near the electrode

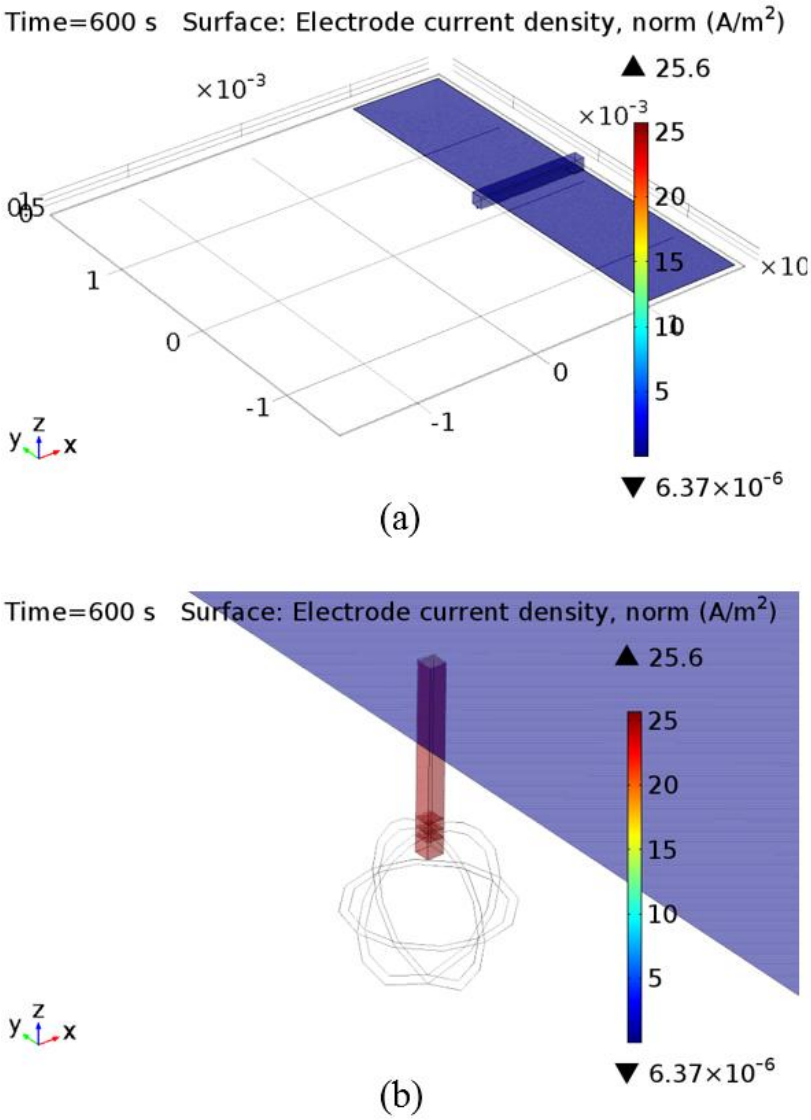

Figure 5-6. Simulated electrode current density of this work (a) whole geometry (a) near the electrode

5.3. PDMS film deflection during assembly process

As mentioned in chapter 5.1, the second factor of current reduction is the deformation of the PDMS chamber by a microtip electrode moving vertically during assembly. In order to analyze the influence of the deformation on the magnitude of the measurement current, the deformation due to the low strength of the thin PDMS film was measured and the effective width in the assembly process was calculated by deformation.

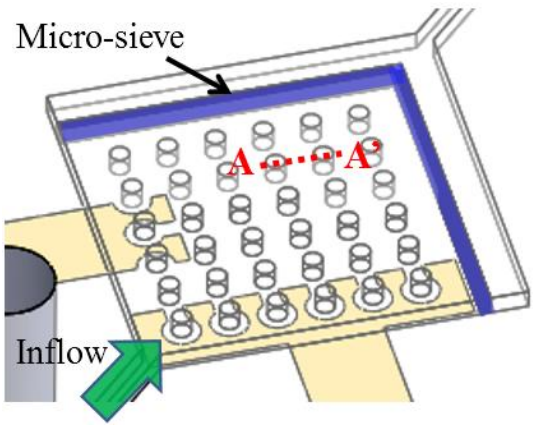

Figure 5-7. Schematic view of PDMS chamber with electrodes

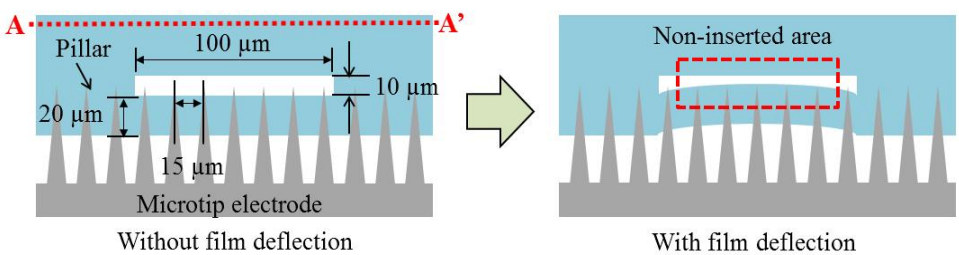

Figure 5-8. Deflection of PDMS film during assembly process

As shown in the above figure, a 100 μm-wide cylindrical pillar at 100 μm distance was fabricated to support 10 μm chamber height between the PDMS ceiling and the 20 μm thick PDMS film in the chamber. However, the force applied

in the vertical direction prevents the microtip from being placed in the chamber as the film rises.

To analyze this phenomenon, the microtip electrode penetrated the PDMS thin film and observed through a microscope as shown below. The left figure below shows the micrograph taken before the electrode is inserted, and the right two figures show the state after the electrode is inserted and placed in the chamber. In the upper right figure, it can be seen that the area where the electrode is inserted after the PDMS thin film is pushed up after insertion is about 28 μm wide.

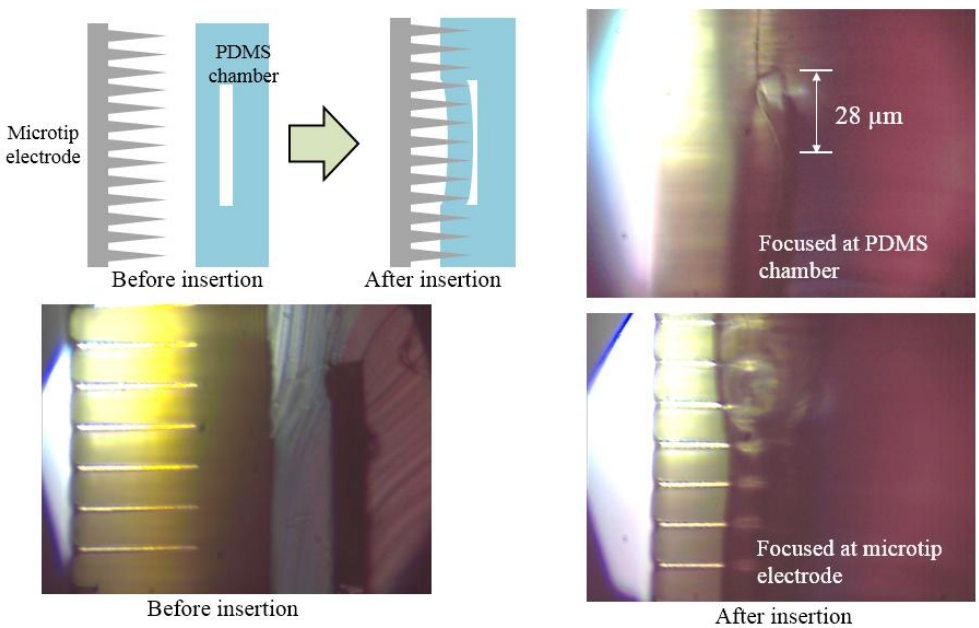

Figure 5-9. Microscope images of PDMS film deflection

In the Figure 5-10, the effective area in which the electrode is inserted into the chamber is calculated. The area of the microtip electrode array is 2 mm × 2 mm and the number of pillar located in the electrode area is 121 in total. As can be seen in the Figure 5-9 and Figure 5-10, the space in which the electrode can be inserted is shaped like a donut around the pillar.

When the thin film is pushed up by the electrode and touches the ceiling, the electrolyte between the microtip electrode and the counter electrode is disconnected. In this case, no current loop is formed even if the cell is inserted into the electrode. Therefore, the space around the inner 81 pillars excluding the outer 40 of 121 pillar is not included in the effective area. The effective area around the outer 40 pillars was calculated as follows.

$$\text{Effective area} = 36 \times \frac{1}{2} \times \pi\{(r+w)^2 - (r)^2\} + 4 \times \frac{1}{4} \times \pi\{(r+w)^2 - (r)^2\} \qquad (5\text{-}15)$$

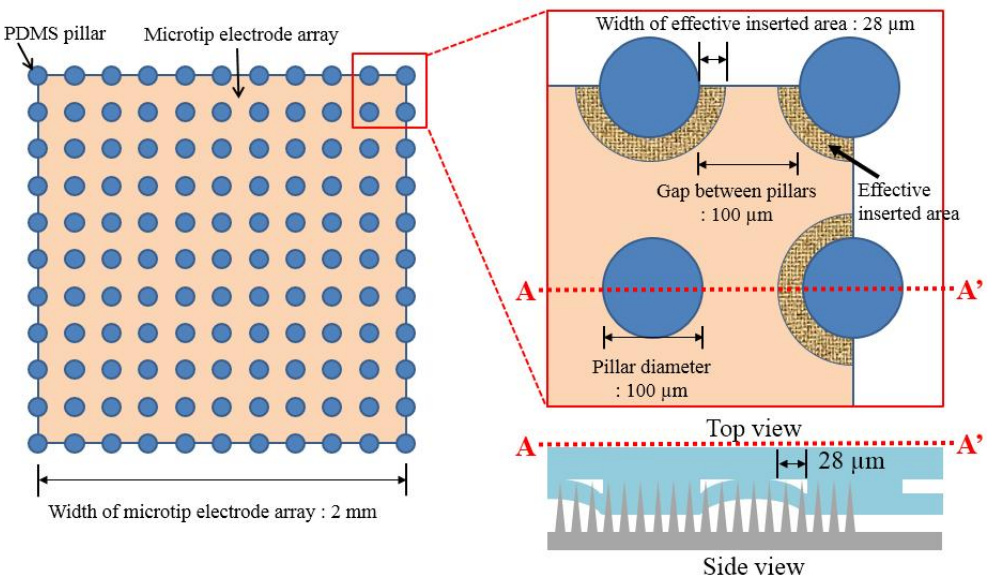

Figure 5-10. Calculation of effective area which is formed around pillars

The effective area obtained by the above equation is divided by the total area, and the ratio of the effective area is shown in the following graph. As the effective area increases around the pillar, the percentage effective area increases. As shown in the Figure 5-9, when the radius of the pillar is 50 μm and the width is 28 μm, the effective area ratio is 5.35%. Since the total number of electrodes is 17689, the number of effective electrodes is 946 when the ratio of the effective area is substituted.

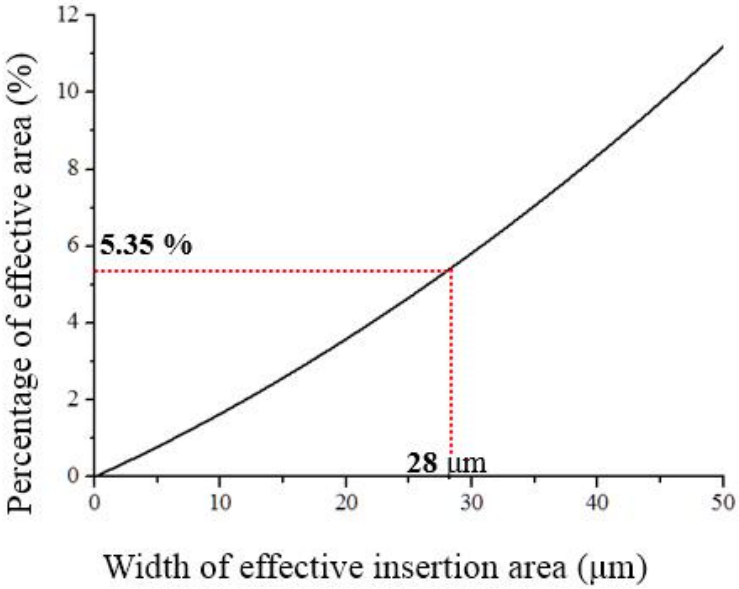

Figure 5-11. Percentage of effective area with width of effective insertion area

When the measured current of 207 pA is divided by the number of effective electrodes of 946, the measured current per electrode is 0.22 pA. This calculation is based on only deformation of the PDMS thin film. In order to consider the reduction of the current due to the distance between the electrodes, the simulation results and the effective area of the Figure 5-4 and Figure 5-10 should be applied.

The simulation values of distance between electrodes from 150 μm to 2150 μm shown in the Figure 5-4 are multiplied by the effective area around the pillar of the distance. If the value is divided by the total effective area, a current value of about 53% is calculated as compared with the case where the distance between electrodes is 5 μm (ideal case). Assuming that the effective electrode has no current loss due to the distance between the electrodes, the current value per electrode is expected to be 0.40 pA. This value is about 34% of the measured value of Stanford University.

Table 5-3. Calculation of current per electrode based on loss analysis

	Value	*Note*
Total microtip electrode number	17689	
Effective microtip electrode number	946	5.35% (effective area calculation)
Current per one electrode	0.22 pA	
Effective current	53%	Calculation with simulation results
Current per one electrode	0.40 pA	34% (Compared to Stanford Univ.)

5.4. Modified design suggestion based on loss analysis

Loss of the measured current is caused by two problems. First, the current loss due to the distance between the working electrode and the counter electrode. As the distance between the working electrode and the counter electrode increases, the magnitude of the current due to the resistance of the electrolyte decreases. The second factor of the current reduction is the deformation of the PDMS chamber by a microtip electrode moving vertically during assembly.

5.4.1. Suggestion of electrode design to reduce the distance between electrodes

As explained in the previous chapter, the current loss becomes smaller the closer the distance between the electrodes. Assuming that the design of the center microtip electrode area is fixed, placing the counter electrode as close as possible to the microtip electrode can reduce the current loss. Unlike the conventional design where the counter electrode is located on one side of the chamber, if the counter electrode is arranged around the four sides of the rectangular area where the microtip electrode is inserted, the current loss can be reduced.

5.4.2. Suggested chamber design to increase effective area

Since the effective area is formed around the pillar, the distance between pillars should be narrowed to increase the rigidity of the thin film to increase the effective area. Because the existing design was designed to have a gap of 100 μm between the pillars, the thin film touched the ceiling of the chamber. This problem prevented the electrodes from being placed in the chamber and the cells in the

chamber were pushed to the other part. As a result, only the electrodes outside the electrode area become effective electrodes and the efficiency is lowered.

The Figure 5-12 and Figure 5-13 are side view photographs of the insertion process of chambers and microtip electrodes with 50 and 30 μm gap between pillars, respectively. In both cases, the thin film did not touch to the ceiling of chamber. When the gap is 30 μm, the degree of squeezing of the chamber in the vertical direction is smaller than that of 50 μm. As a result, the inserted electrode can be positioned more easily in the chamber, and the effective area can be widened because the cells do not escape.

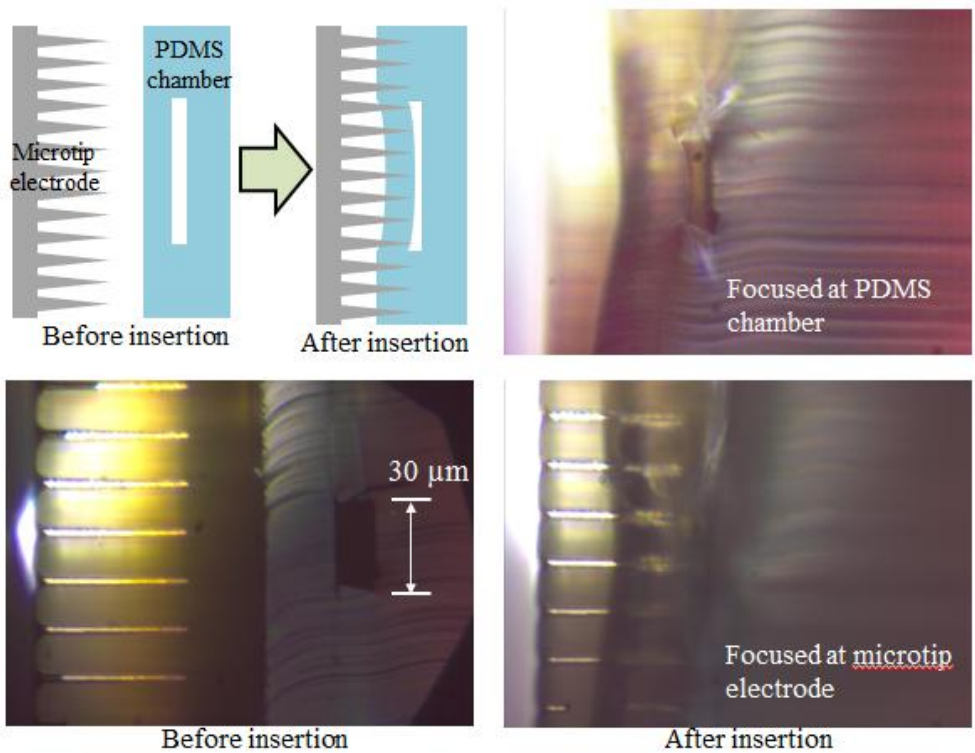

Figure 5-12. A side vew microscope photograph showing the insertion process of the chamber and microtip electrode with 30 μm gap between pillar

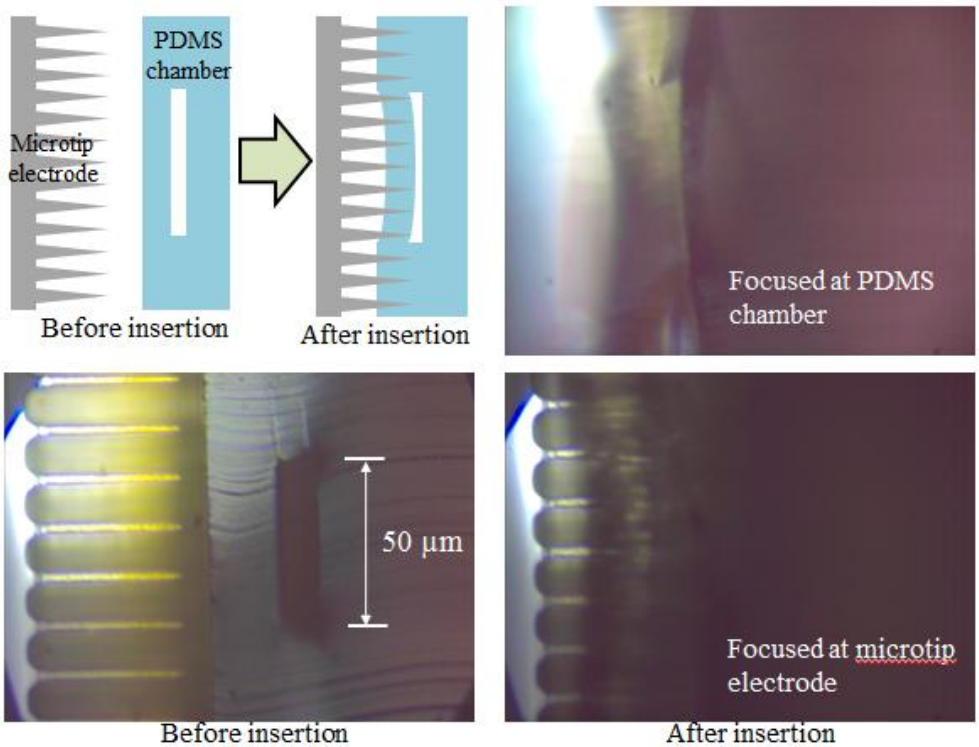

Figure 5-13. A side vew microscope photograph showing the insertion process of the chamber and microtip electrode with 50 μm gap between pillar

The Figure 5-14 shows that the percentage of the effective area increases as the width of effective insertion area increases when the gap between pillars is 100 μm, 50 μm, and 30 μm. In the figure, only the effective area around the outer pillars was calculated. In the case of the gap between pillars is 100 μm, increasing the width can achieve the highest effective area percentage. However, when the width is limited, the gap between pillars of 30 μm has a relatively high effective area.

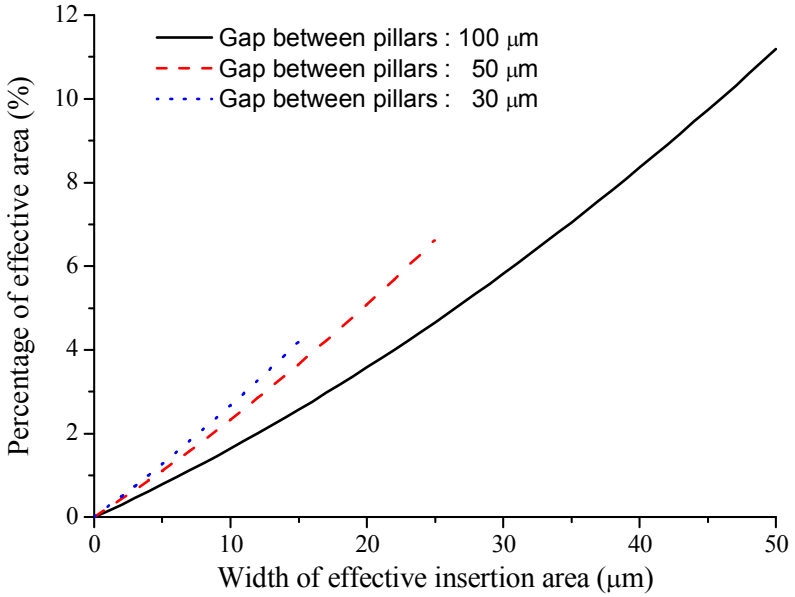

Figure 5-14. The percentage of the effective area as the width of effective insertion area increases when the spacing between pillars is 100 μm, 50 μm, 30 μm

The Figure 5-15 shows that the percentage of the effective area to the width of effective insertion area increases when the effective area extends to the inside of the electrode area. Assuming that the width is 28 μm as shown in the Figure 5-9, it is calculated that the effective area ratio is 75.5% and 91.1% when the spacing between pillars is 50 μm and 30 μm, respectively.

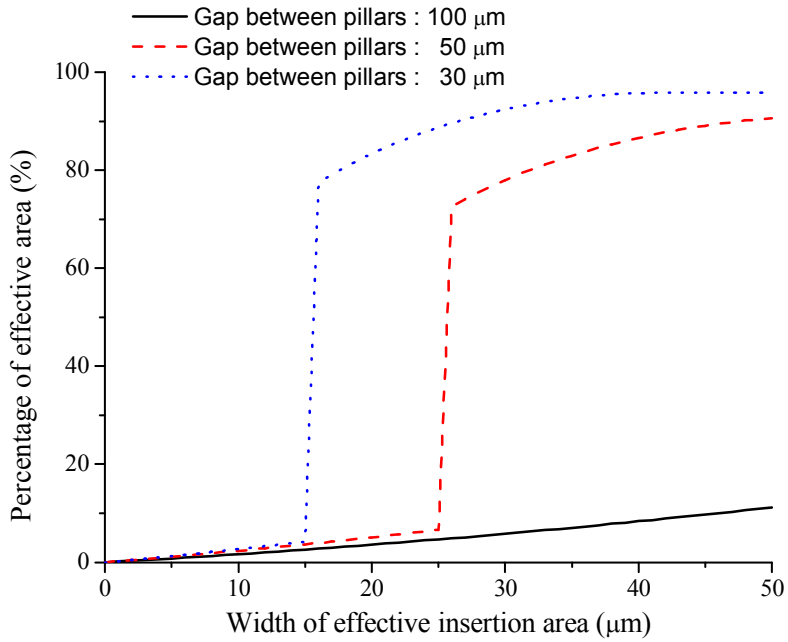

Figure 5-15. The percentage of the effective area when the effective area extends to the inside of the electrode area

Chapter 6. Conclusion

Microbial fuel cell using an array of ultramicroelectrode (UME) on invasive silicon microtips has been designed and fabricated using a microfluidic chamber and a microtip electrode array. A microtip electrode array with localized UMEs on the tip ends has been demonstrated and characterized with CV measurements in an electrolyte. A combination of DRIE and RIE processes has been introduced to fabricate a high-aspect-ratio microtip with a small apex radius of tens of nanometers. The details of the fabrication process and the results associated with the formation of the microtip with a high aspect ratio and small apex radius have been investigated. The aspect ratio and the apex radius of the microtip are related to the characteristics of the etching mask geometry, such as the diameter and the gap between patterns. Localized UMEs at the tip ends were formed using the RIE etching process with a low selectivity ratio between the photoresist and insulation layer, without an additional photolithography step.

Photosynthetic algal cells are assembled with microfluidic devices by inserting microtip electrode into PDMS fluidic devices. The sharp tip of the fabricated microtip electrode is located in the channel by penetrating the bottom thin film of the PDMS fluid channel. The microtip electrode was designed to have an aspect ratio of 5 and a tip radius of 50 nm or less to facilitate penetration of the PDMS thin film. An alignment layer capable of adjusting the microtip electrode position in the channel was fabricated around the microtip electrode array.

Short circuit current and open circuit voltage of the inserted electrode array were measured at 207 pA and 26 mV. The measured current were lower than the expected values, due to the decrease of the measured current due to the distance

between the working electrode and the counter electrode and deformation of the PDMS thin film by the micro probe electrode moving in the vertical direction during the inserting process. The number of effective electrodes is 946, the measured current per electrode is 0.22 pA. The current value of about 53% is calculated as compared with the case where the distance between electrodes is 5 μm (ideal case). Assuming that the effective electrode has no current loss due to the distance between the electrodes, the current value per electrode is expected to be 0.40 pA. This value is about 34% of the measured value of Stanford University.

This dissertation demonstrated the possibility of intracellular insertion of the electrode using the developed microtip electrode and the proposed through-polydimethylsiloxane assembly method. In addition, a short circuit current and an open circuit voltage measurement showed the possibility of being used as a microbial fuel cell.

Two methods have been proposed to reduce the current loss. First, by reducing the distance between the electrodes, the current loss due to the resistance of the electrolyte can be reduced. Second, if the spacing between the pillars is reduced, the effective area in the chamber and the number of effective electrodes can be increased. These two proposals make it possible to reduce the current loss and increase the efficiency of the microbial fuel cell.

Reference

[1] Z. Du, H. Li, and T. Gu, "A state of the art review on microbial fuel cells: a promising technology for wastewater treatment and bioenergy," *Biotechnology advances,* vol. 25, pp. 464-482, 2007.

[2] B. E. Logan and J. M. Regan, "Electricity-producing bacterial communities in microbial fuel cells," *TRENDS in Microbiology,* vol. 14, pp. 512-518, 2006.

[3] M. Rosenbaum and U. Schröder, "Photomicrobial solar and fuel cells," *Electroanalysis,* vol. 22, pp. 844-855, 2010.

[4] D. H. Park and J. G. Zeikus, "Electricity generation in microbial fuel cells using neutral red as an electronophore," *Applied and environmental microbiology,* vol. 66, pp. 1292-1297, 2000.

[5] J. Jiang, Q. Zhao, J. Zhang, G. Zhang, and D.-J. Lee, "Electricity generation from bio-treatment of sewage sludge with microbial fuel cell," *Bioresource Technology,* vol. 100, pp. 5808-5812, 2009.

[6] B. E. Logan, B. Hamelers, R. Rozendal, U. Schröder, J. Keller, S. Freguia, *et al.*, "Microbial fuel cells: methodology and technology," *Environmental science & technology,* vol. 40, pp. 5181-5192, 2006.

[7] S. Cheng and B. E. Logan, "Ammonia treatment of carbon cloth anodes to enhance power generation of microbial fuel cells," *Electrochemistry Communications,* vol. 9, pp. 492-496, 2007.

[8] E. HaoYu, S. Cheng, K. Scott, and B. Logan, "Microbial fuel cell performance with non-Pt cathode catalysts," *Journal of Power Sources,* vol. 171, pp. 275-281, 2007.

[9] H. Liu and B. E. Logan, "Electricity generation using an air-cathode single

chamber microbial fuel cell in the presence and absence of a proton exchange membrane," *Environmental science & technology,* vol. 38, pp. 4040-4046, 2004.

[10] H. Liu, R. Ramnarayanan, and B. E. Logan, "Production of electricity during wastewater treatment using a single chamber microbial fuel cell," *Environmental science & technology,* vol. 38, pp. 2281-2285, 2004.

[11] B. Logan, S. Cheng, V. Watson, and G. Estadt, "Graphite fiber brush anodes for increased power production in air-cathode microbial fuel cells," *Environmental science & technology,* vol. 41, pp. 3341-3346, 2007.

[12] J. R. Kim, S. Cheng, S.-E. Oh, and B. E. Logan, "Power generation using different cation, anion, and ultrafiltration membranes in microbial fuel cells," *Environmental Science & Technology,* vol. 41, pp. 1004-1009, 2007.

[13] K. Watanabe, "Recent developments in microbial fuel cell technologies for sustainable bioenergy," *Journal of bioscience and bioengineering,* vol. 106, pp. 528-536, 2008.

[14] G.-C. Gil, I.-S. Chang, B. H. Kim, M. Kim, J.-K. Jang, H. S. Park*, et al.*, "Operational parameters affecting the performannce of a mediator-less microbial fuel cell," *Biosensors and Bioelectronics,* vol. 18, pp. 327-334, 2003.

[15] R. A. Rozendal, H. V. Hamelers, and C. J. Buisman, "Effects of membrane cation transport on pH and microbial fuel cell performance," *Environmental science & technology,* vol. 40, pp. 5206-5211, 2006.

[16] K. J. Chae, M. Choi, F. F. Ajayi, W. Park, I. S. Chang, and I. S. Kim, "Mass transport through a proton exchange membrane (Nafion) in microbial fuel cells," *Energy & Fuels,* vol. 22, pp. 169-176, 2007.

[17] D. P. Strik, R. A. Timmers, M. Helder, K. J. Steinbusch, H. V. Hamelers, and C. J. Buisman, "Microbial solar cells: applying photosynthetic and electrochemically active organisms," *Trends in biotechnology,* vol. 29, pp. 41-49, 2011.

[18] C. Spindt, C. Holland, A. Rosengreen, and I. Brodie, "Field-emitter arrays for vacuum microelectronics," *IEEE Transactions on Electron Devices,* vol. 38, pp. 2355-2363, 1991.

[19] P.-A. Auroux, D. Iossifidis, D. R. Reyes, and A. Manz, "Micro total analysis systems. 2. Analytical standard operations and applications," *Analytical chemistry,* vol. 74, pp. 2637-2652, 2002.

[20] D. R. Reyes, D. Iossifidis, P.-A. Auroux, and A. Manz, "Micro total analysis systems. 1. Introduction, theory, and technology," *Analytical chemistry,* vol. 74, pp. 2623-2636, 2002.

[21] *photosynthesis*. Available: https://upload.wikimedia.org/wikipedia/commons/4/49/Thylakoid_membrane_3.svg

[22] V. Flexer and N. Mano, "From dynamic measurements of photosynthesis in a living plant to sunlight transformation into electricity," *Analytical chemistry,* vol. 82, pp. 1444-1449, 2010.

[23] Y. Furukawa, T. Moriuchi, and K. Morishima, "Design principle and prototyping of a direct photosynthetic/metabolic biofuel cell (DPMFC)," *Journal of Micromechanics and Microengineering,* vol. 16, p. S220, 2006.

[24] F. Qian, G. Wang, and Y. Li, "Solar-driven microbial photoelectrochemical cells with a nanowire photocathode," *Nano letters,* vol. 10, pp. 4686-4691, 2010.

[25] M. Rosenbaum, U. Schröder, and F. Scholz, "Utilizing the green alga Chlamydomonas reinhardtii for microbial electricity generation: a living solar cell," *Applied microbiology and biotechnology,* vol. 68, pp. 753-756, 2005.

[26] N. Sekar and R. P. Ramasamy, "Recent advances in photosynthetic energy conversion," *Journal of Photochemistry and Photobiology C: Photochemistry Reviews,* vol. 22, pp. 19-33, 2015.

[27] M. Chiao, K. B. Lam, and L. Lin, "Micromachined microbial and photosynthetic fuel cells," *Journal of Micromechanics and Microengineering,* vol. 16, p. 2547, 2006.

[28] W. Ryu, S.-J. Bai, J. S. Park, Z. Huang, J. Moseley, T. Fabian*, et al.*, "Direct extraction of photosynthetic electrons from single algal cells by nanoprobing system," *Nano letters,* vol. 10, pp. 1137-1143, 2010.

[29] D. J. Harrison, K. Fluri, K. Seiler, Z. Fan, C. S. Effenhauser, and A. Manz, "Micromachining a miniaturized capillary electrophoresis-based chemical analysis system on a chip," *SCIENCE-NEW YORK THEN WASHINGTON-,* vol. 261, pp. 895-895, 1993.

[30] P. Wilding, J. Pfahler, H. H. Bau, J. N. Zemel, and L. J. Kricka, "Manipulation and flow of biological fluids in straight channels micromachined in silicon," *Clinical Chemistry,* vol. 40, pp. 43-47, 1994.

[31] D. C. Duffy, J. C. McDonald, O. J. Schueller, and G. M. Whitesides, "Rapid prototyping of microfluidic systems in poly (dimethylsiloxane)," *Analytical chemistry,* vol. 70, pp. 4974-4984, 1998.

[32] J. C. McDonald and G. M. Whitesides, "Poly (dimethylsiloxane) as a material for fabricating microfluidic devices," *Accounts of chemical*

research, vol. 35, pp. 491-499, 2002.

[33] D. Di Carlo, N. Aghdam, and L. P. Lee, "Single-cell enzyme concentrations, kinetics, and inhibition analysis using high-density hydrodynamic cell isolation arrays," *Analytical chemistry,* vol. 78, pp. 4925-4930, 2006.

[34] J. R. Rettig and A. Folch, "Large-scale single-cell trapping and imaging using microwell arrays," *Analytical chemistry,* vol. 77, pp. 5628-5634, 2005.

[35] M. Yang, C.-W. Li, and J. Yang, "Cell docking and on-chip monitoring of cellular reactions with a controlled concentration gradient on a microfluidic device," *Analytical chemistry,* vol. 74, pp. 3991-4001, 2002.

[36] N. Bao and C. Lu, "A microfluidic device for physical trapping and electrical lysis of bacterial cells," *Applied Physics Letters,* vol. 92, p. 214103, 2008.

[37] M. B. Kerby, R. S. Legge, and A. Tripathi, "Measurements of kinetic parameters in a microfluidic reactor," *Analytical chemistry,* vol. 78, pp. 8273-8280, 2006.

[38] J. Kim, J. Heo, and R. M. Crooks, "Hybridization of DNA to bead-immobilized probes confined within a microfluidic channel," *Langmuir,* vol. 22, pp. 10130-10134, 2006.

[39] M.-S. Kim, S. I. Cho, K.-N. Lee, and Y.-K. Kim, "Fabrication of microchip electrophoresis devices and effects of channel surface properties on separation efficiency," *Sensors and Actuators B: Chemical,* vol. 107, pp. 818-824, 2005.

[40] M.-S. Kim, J.-H. Kim, Y.-S. Lee, G.-G. Lim, H.-B. Lee, J.-H. Park*, et al.*,

"Experimental and theoretical analysis of DEP-based particle deflection for the separation of protein-bound particles," *Journal of Micromechanics and Microengineering,* vol. 19, p. 015029, 2008.

[41] M. J. Schöning, M. Jacobs, A. Muck, D.-T. Knobbe, J. Wang, M. Chatrathi, *et al.*, "Amperometric PDMS/glass capillary electrophoresis-based biosensor microchip for catechol and dopamine detection," *Sensors and Actuators B: Chemical,* vol. 108, pp. 688-694, 2005.

[42] N. Triroj, M. A. Lapierre-Devlin, S. O. Kelley, and R. Beresford, "Microfluidic three-electrode cell array for low-current electrochemical detection," *IEEE Sensors Journal,* vol. 6, pp. 1395-1402, 2006.

[43] J. Park, J.-h. Chang, M. Choi, J. J. Pak, D.-Y. Lee, and Y. K. Pak, "Microfabirated clark-type sensor for measuing dissolved oxygen," in *Sensors, 2007 IEEE*, 2007, pp. 1412-1415.

[44] V. T. Binh and J. Marien, "Characterization of microtips for scanning tunneling microscopy," *Surface science,* vol. 202, pp. L539-L549, 1988.

[45] J. L. Amphlett and G. Denuault, "Scanning electrochemical microscopy (SECM): an investigation of the effects of tip geometry on amperometric tip response," *The Journal of Physical Chemistry B,* vol. 102, pp. 9946-9951, 1998.

[46] N. A. Aziz and B. Y. Majlis, "Fabrication study of solid microneedles array using HNA," in *2006 IEEE International Conference on Semiconductor Electronics*, 2006, pp. 20-24.

[47] Y. Hanein, C. G. Schabmueller, G. Holman, P. Lücke, D. D. Denton, and K. F. Böhringer, "High-aspect ratio submicrometer needles for intracellular applications," *Journal of Micromechanics and Microengineering,* vol. 13, p.

S91, 2003.

[48] H. Sasaki, M. Shikida, and K. Sato, "Fabrication of densely arrayed Si needles with large height for transdermal drug delivery system application," *IEEJ Transactions on Electrical and Electronic Engineering,* vol. 2, pp. 340-347, 2007.

[49] R. Bhandari, S. Negi, L. Rieth, R. Normann, and F. Solzbacher, "A novel method of fabricating convoluted shaped electrode arrays for neural and retinal prostheses," *Sensors and Actuators A: Physical,* vol. 145, pp. 123-130, 2008.

[50] J.-G. Ha, J.-H. Park, S.-J. Bai, Y.-K. Kim, and S.-K. Lee, "Fabrication and measurements of high aspect ratio conductive microtip array with localized ultra-micro electrode at the tip end," in *Micro Electro Mechanical Systems (MEMS), 2012 IEEE 25th International Conference on*, 2012, pp. 235-238.

[51] B. Volland, H. Heerlein, I. Kostic, and I. Rangelow, "The application of secondary effects in high aspect ratio dry etching for the fabrication of MEMS," *Microelectronic engineering,* vol. 57, pp. 641-650, 2001.

[52] K. Leonhardt, A. Avdic, A. Lugstein, I. Pobelov, T. Wandlowski, M. Wu*, et al.*, "Atomic force microscopy-scanning electrochemical microscopy: influence of tip geometry and insulation defects on diffusion controlled currents at conical electrodes," *Analytical chemistry,* vol. 83, pp. 2971-2977, 2011.

[53] *Synechococcus*. Available: https://utex.org/products/utex-l-2973

[54] *Haematococcus*. Available: https://algaeexpert.com/product/haematococcus-pluvalis-3/

[55] *Microcystis*. Available:

http://protist.i.hosei.ac.jp/PDB/Images/Prokaryotes/Chroococcaceae/Microcystis/sp_02.html

[56] J. Komadina, S. Walch, R. Fasching, A. Grossman, and F. B. Prinz, "Reversible oxidation of spinach ferredoxin at surface-modified electrodes," *Journal of The Electrochemical Society,* vol. 155, pp. B1008-B1012, 2008.

[57] S. Okayama, "Redox potential of plastoquinone A in spinach chloroplasts," *Biochimica et Biophysica Acta (BBA)-Bioenergetics,* vol. 440, pp. 331-336, 1976.

[58] J. Franklin, "Plant Growth Chamber Handbook. (Iowa Agriculture and Home Economics Experiment Station Special Report No. 99 (SR-99) and North Central Regional Research Publication No. 340.). Ed. by R. W. LANGHANS and T. W. TIBBITS. 21×27·5 cm. Pp. viii+240 with 20 tables and 45 text-figures. Ames, IA, USA: Iowa State University, 1997. Price p/b: $15.00, ISBN 0361 199X," *New Phytologist,* vol. 138, pp. 743-750, 1998.

[59] M. Tominaga, S. Hashimoto, A. Misaka, and N. Nakashima, "Thermal Stability and Electrode Reaction of Chlorella Ferredoxin Embedded in Artificial Lipid Bilayer Membrane Films on a Graphite Electrode," *Analytical Chemistry,* vol. 71, pp. 2790-2796, 1999/07/01 1999.

[60] P. Wanichapichart, S. Bunthawin, A. Kaewpaiboon, and K. Kanchanapoom, "Determination of cell dielectric properties using dielectrophoretic technique," *ScienceAsia,* vol. 28, pp. 113-119, 2002.

국문 초록

본 논문은 광합성 연료 전지에의 응용이 가능한 폴리디메틸실록세인 관통 미세 탐침 전극 어레이의 개발에 관한 것이다. 본 연구에서는 종래의 광합성 세포 하나에 전극을 삽입하여 전류를 뽑아내는 방식에서 가지는 단점인 효율성 낮은 전력 추출을 극복하기 위해 미세 탐침 전극과 미세 유체 소자 제작 기술을 이용하여 적층된 세포 어레이에서 전력을 추출하는 것을 목표로 하였다.

이를 위해서 미세 유체 소자 내에 적층된 광합성 세포 내에 탐침 형태의 전극 어레이를 삽입시키는 방법이 제안되었다. 미세 탐침 전극은 실리콘 이방성/등방성 식각 공정의 조합을 통해 제작된다. 이방성 식각 공정을 통해 제작된 실리콘 기둥은 등방성 식각 공정에서 측벽 식각 속도의 변화에 따라 기둥 형태에서 탐침 형태로 변화한다. 실리콘 미세 탐침의 종횡비와 탐침 끝 반지름은 식각 마스크 패턴의 직경과 간격을 변화시킨 마스크 설계에 의해 제어된다. 전도층과 절연층의 증착/식각 공정을 통해 탐침 끝부분에 전극을 형성하고 전기화학적 측정을 통하여 전극으로서의 성능을 검증하였고 원추형의 미세 전극 이론에 근거한 평가와 비교하였다.

광합성 조류 세포는 PDMS 유체 소자 중에 미세 탐침 전극을 삽입하는 방법으로 마이크로 유체 소자와 결합된다. 제작된 미세 탐침 전극의 날카로운 끝 부분이 PDMS 유체 채널의 하단 박막을 관통시킴으로써 채널 내에 위치하게 된다. PDMS 박막을 관통하기

용이하도록 전극의 끝 부분은 종횡비 5 이상, 탐침 끝 반지름이 50 nm이하로 제작되었다. 제작된 탐침 전극 주위에는 채널 내의 탐침 위치를 조절할 수 있는 정렬 층을 제작하여 채널 내에 배치되도록 설계되었다.

삽입된 전극 어레이의 단락 전류와 개방 회로 전압은 207 pA, 26 mV로 측정되었다. 측정된 전류 값에 대한 손실 분석은 두 가지 방법으로 진행되었다. 첫째, 작동 전극과 상대 전극간의 거리에 의한 측정 전류의 감소를 전기화학 시뮬레이션을 통해 검증하였다. 작동 전극과 상대 전극의 거리가 멀어질수록 전해질의 저항에 의한 전류의 크기는 감소하게 된다. 둘째, 삽입 과정에서 수직 방향으로 움직이는 미세 탐침 전극에 의한 PDMS 박막의 변형이다. 변형이 측정 전류의 크기에 미치는 영향을 분석하기 위해 얇은 두께의 PDMS 박막의 낮은 강도에 의한 변형을 측정하고 변형에 의해 삽입 과정에서의 유효 넓이를 계산하였다.

시뮬레이션 결과를 통해 전극 간 거리가 5um인 경우 (이상적인 값)에 비해 약 53 %의 전류 값이 측정된 것으로 계산되었다. 유효 면적 계산을 반영한 결과, 전체 전극 개수 17689개 중 유효 전극 개수는 946개이고, 전극 1개당 측정 전류는 0.22 pA이다. 만약 유효 전극이 전극 간 거리에 의한 전류 손실이 없다고 가정한다면 전극 1개당 전류 값은 0.40 pA로 계산된다. 이 값은 Stanford Univ.의 측정값과 비교해서 약 34 %의 값을 가진다.

결론적으로, 본 논문에서는 개발된 미세 탐침 전극과 제안된

폴리디메틸실록세인 관통 삽입 방법을 이용하여 전극의 세포 내 삽입의 가능성을 보였다. 그리고 단락 전류와 개방 회로 전압 측정을 통해 미생물 연료 전지로서의 사용 가능성을 보였으며, 측정된 결과의 손실 분석을 바탕으로 전극 배치와 미세 유로 구조의 개선을 통해 전류 손실을 줄일 수 있는 방법을 제시하였다.